Covariation of airborne biogenic tracers (CO_2, COS, and CO) supports stronger than expected growing season photosynthetic uptake in the southeastern US

Nicholas Parazoo[1], Kevin Bowman[1], Bianca Baier[2,3], Junjie Liu[1], Meemong Lee[1], Le Kuai[1], Yoichi Shiga[4], Ian Baker[5], Mary Whelan[6], Sha Feng[7,8], Maarten Krol[9,10], Colm Sweeney[3], Kenneth J. Davis[7,8]

[1]Jet Propulsion Laboratory, California Institute of Technology, Pasadena, CA, USA

[2]Cooperative Institute for Research in Environmental Sciences, University of Colorado-Boulder, Boulder, CO, USA

[3]NOAA Earth System Research Laboratory Global Monitoring Division, Boulder, CO, USA,

[4]Universities Space Research Association, Moffett Field, CA, USA

[5]Cooperative Institute for Research in the Atmosphere, Colorado State University, Fort Collins, Colorado, USA

[6]Department of Environmental Sciences, Rutgers, The State University of New Jersey, New Brunswick, New Jersey

[7]Department of Meteorology and Atmospheric Science, Pennsylvania State University, University Park, PA, USA

[8]Earth and Environmental Systems Institute, Pennsylvania State University, University Park, PA, USA

[9]Institute for Marine and Atmospheric Research, Utrecht University, Utrecht, the Netherlands

[10]Meteorology and Air Quality, Wageningen University & Research, Wageningen, the Netherlands

Abstract

The ACT-America Earth Venture mission conducted five airborne campaigns across four seasons from 2016-2019, to study the transport and fluxes of Greenhouse gases across the eastern United States (US). Unprecedented spatial sampling of atmospheric tracers (CO_2, CO, and COS) related to biospheric processes offers opportunities to improve our qualitative and quantitative understanding of seasonal and spatial patterns of biospheric carbon uptake.

Here, we examine co-variation of boundary layer enhancements of CO_2, CO, and COS across three diverse regions: the crop-dominated Midwest, evergreen-dominated South, and deciduous broadleaf-dominated Northeast. To understand the biogeochemical processes controlling these tracers, we compare the observed co-variation to simulated co-variation resulting from model- and satellite- constrained surface carbon fluxes. We found indication of a common terrestrial biogenic sink of CO_2 and COS and secondary production of CO from biogenic sources in summer throughout the eastern US. Stomatal conductance likely drives fluxes through diffusion of CO_2 and COS into leaves and emission of biogenic volatile organic compounds into the atmosphere.

ACT-America airborne campaigns filled a critical sampling gap in the southern US, providing information about seasonal carbon uptake in southern temperate forests, and demanding a deeper investigation of underlying biological processes and climate sensitivities. Satellite- constrained carbon fluxes capture much of the observed seasonal and spatial variability, but underestimate the magnitude of net CO_2 and COS depletion in the Southeast, indicating a stronger than expected net sink in late summer.

1. Introduction

The global terrestrial biosphere has removes 20% of fossil emissions from the atmosphere (Arneth et al., 2017). The exact spatial distribution and underlying drivers of the terrestrial carbon sink has been a matter of debate for decades, but it is generally agreed to be split between the tropics and northern extra-tropics and driven by a combination of nutrient (CO_2, N) fertilization, thermal fertilization, and land cover / land use change (Stephens et al., 2007; Schimel et al., 2015; Madani et al., 2020; Liu et al., 2020a). Global top-down inversion studies leveraging surface-based CO_2 stations in northern latitudes (CarbonTracker, CT2019) indicate

strong and persistent CO_2 uptake in North America (NA) of ~0.6 Gt C yr-1 from 2001-2018 (https://www.esrl.noaa.gov/gmd/ccgg/carbontracker/), driven by temperate ecosystems in the eastern US (east of the Rockies) and in southern Canada (Peters et al., 2007). Recent inversion efforts that incorporate satellite-based CO_2 observations support these estimates for temperate eastern North America, showing a statistically significant sink of similar magnitude (~0.5 Pg C) over the period 2010-2018 (Liu et al., 2020b). These results are encouraging as we move toward combined surface- and satellite-based inversion approaches to improve spatially and temporally integrated constraints of net CO_2 exchange at regional and global scale, and advance regional-scale understanding of terrestrial CO_2 sinks (e.g., Byrne et al., 2020a,b).

Airborne strategies focused on multi-tracer vertical profiles within continental interiors offer additional opportunities for studying spatially variable sources and sinks. Intensive airborne campaigns enable long-distance transect flights needed to sample multiple air masses across biologically diverse regions, sometimes multiple times per day, at spatial scales ranging from 100-1000 km. Moreover, airborne campaigns that fly into and out of the atmospheric boundary layer can sample air immediately in contact with the surface for increased sensitivity to local processes, as well as provide periodic sampling of background air in the free troposphere, thus accounting for the influence of long-range transport (Parazoo et al., 2016; Baier et al, 2020). These flight strategies provide a critical advantage over column integrated satellite data, and fixed-point tower data, by directly measuring spatial gradients in anthropogenic and biogenic land surface influence.

Key to disentangling multiple anthropogenic and biogenic CO_2 sources and sinks (agricultural activity, forest productivity, biomass burning, gas and oil extraction and consumption) is multi-species sampling. Carbon monoxide (CO) and Carbonyl Sulfide (COS) are increasingly important atmospheric constituents for tracking biogenic activity and gross primary productivity (GPP; Campbell et al., 2008; Hudman et al., 2008). Plant uptake of atmospheric CO_2 and COS are directly related to photosynthesis through stomatal conductance (Campbell et al., 2008; Berry et al., 2013). While the main source of atmospheric CO is incomplete combustion of biomass and fossil fuel, and subsequent oxidation of hydrocarbons, a nontrivial secondary source is biogenic volatile organic compounds (BVOCs) emitted from vegetation, which oxidize to produce CO accounting for ~18% of the global CO budget (Worden et al., 2019). In the absence of biomass

86 burning and continued CO emissions from anthropogenic sources, the relative importance of
87 secondary CO production increases.

88 Airborne COS and CO observations provide a unique opportunity to more directly study
89 biogeochemical processes related at multiple temporal and spatial scales. Boundary layer CO
90 data collected during the ICARTT aircraft campaign in the eastern US in summer 2004 revealed
91 strong emissions from isoprene sources centered in the Southeast US, which exceeded regionally
92 integrated anthropogenic emissions that peak in the Northeast near the strongest combustion
93 sources (Hudman et al., 2008). Vertical COS profiles collected from the NOAA / Global
94 Monitoring Laboratory (GML) light aircraft network from 2005-2012 indicate a hotspot of
95 growing season GPP arising from intense agricultural activity in the upper Midwest US,
96 exceeding all other regions in the US (Hilton et al., 2017). This hotspot is consistent with
97 satellite-based measurements of solar induced fluorescence (SIF), another important signal of
98 biogenic activity and in particular the light reactions of photosynthesis (Guanter et al., 2014).
99 Crops are also implicated in the large seasonal, regional depletion in BL CO_2 observed by towers
100 (Miles et al, 2012) and the large net annual CO_2 fluxes inferred from those tower data (Schuh et
101 al, 2013). Ecosystem model simulations of GPP show a range of spatial patterns in the eastern
102 US, and only a subset of models are consistent with strong crop uptake in the Midwest inferred
103 from SIF and COS (Guanter et al., 2014; Hilton et al., 2017). Multi-tracer data thus provide
104 important proxies for studying spatial GPP variability, and offer unique benchmarks for
105 improving model formulations of agricultural productivity, light capture by leaves, and CO_2
106 diffusion by stomatal conductance (Hilton et al., 2018; Whelan et al., 2020).

107 Atmospheric Carbon and Transport (ACT) – America, is a NASA Earth Venture Suborbital
108 airborne mission that targeted multi-species vertical profiles in the eastern US for improved
109 understanding of CO_2 sources and sinks (Davis et al, submitted; Wei et al, submitted). ACT-
110 America conducted five airborne campaigns across four seasons from 2016-2019, capturing
111 vertical gradients of CO_2, CO, and COS across three unique regions including the humid sub-
112 tropical, evergreen-dominated South, seasonally warm- to hot- crop-dominated Midwest, and the
113 warm temperate, deciduous broadleaf forest dominated Northeast. A subset of ACT-America
114 flights was coordinated with satellite overpasses from the Orbiting Carbon Observatory (OCO-
115 2), providing simultaneous measurements of column-integrated atmospheric CO_2 and underlying
116 SIF. The combination of ACT-America, OCO-2, and existing airborne measurement networks

from NOAA/GML (Sweeney et al., 2015) provides an unprecedented wealth of information about biological processes driving CO_2 uptake across the central and eastern US.

Here, we present a first interpretation of ACT-America tracer-tracer distributions, and their co-variation, across the central and eastern US. We focus on three biologically-sensitive tracer species (CO_2, CO, and COS), which are collected periodically in airborne flask samples (~10-50 samples per region and campaign), and co-analyzed in the laboratory, providing high precision measurements collocated in space and time. We analyze the seasonal distribution of individual species, and their covariation, across the three unique ACT regions (Northeast, Midwest, and South) to gain a better understanding of the seasonal and spatial distribution of net CO_2 sources and sinks, and the underlying biogenic and anthropogenic drivers.

To facilitate interpretation of observed tracer distributions, we also analyze predicted signals obtained from high resolution atmospheric simulations forced by spatially-explicit surface fluxes of CO_2, COS, and CO. We examine "top-down" fluxes from inverse methods constrained by multiple observational data-streams, and "bottom-up" model estimates, representing climatological prior fluxes going into inverse methods. We thus use predicted signals to link observed tracer distributions to spatial patterns in biogenic and anthropogenic driven surface fluxes, evaluate the state of bottom-up prior fluxes and information gain from inversion systems, and learn about "missing processes" from the residual of ACT-America comparisons.

This study has three main objectives: (1) first interpretation of ACT-America tracer-tracer covariation, (2) examination of underlying surface flux drivers across diverse regions in the central and eastern US, and (3) evaluation of observed vs expected surface flux patterns, providing insight into processes that are missing from models. We accomplish these objectives in three main steps: (1) Establish observed correlation patterns between CO_2, CO, and COS (*Section 2.1*), (2) Provide satellite constrained estimates of surface fluxes of CO_2, CO, and COS accounting for multiple carbon sources and sinks including terrestrial and oceanic biological exchange, biomass burning and anthropogenic emissions (*Section 2.2*), (3) Convolve posterior surface fluxes with surface influence functions for attribution of observed correlation patterns (*Section 2.3*). We also use simulation experiments to evaluate the use of airborne free troposphere data to account for background influences from boundary layer data (*Text S1*). By

using a model-data analysis framework, this study provides a deeper investigation into the processes driving observed CO_2 patterns.

2. Methods

2.1 ACT-America Tracer Observations

High quality CO_2, CO, and COS trace gas mole fractions are collected *in situ* from two instrumented aircraft platforms, the NASA Langley Beechcraft B200 King Air and the NASA Goddard Space Flight Center's C-130 Hercules (Davis et al., 2018). The data are derived from laboratory measurements of whole air samples collected by Programmable Flask Package (PFP) onboard the two ACT-America aircraft (Bair et al., 2020). The two aircraft conducted five six-week field campaigns spanning the Central and Eastern US (27°S-49°N, 106°W-73°W) covering all four seasons from 2016 through 2019, including late summer 2016 (July-August), winter 2017 (February-March), fall 2017 (October-November), spring 2018 (April-May), and early summer 2019 (June-July). Each campaign focused on sampling three unique regions, which are defined here as Northeast (NE: 35-45°N, 85-75°W), Midwest (MW: 37-45°N, 100-87°W), and South (~28-37°N, 100-85°W). These regions (and corresponding flask samples) are shown in Figure 1, and color coded as blue, red, and green for the remainder of the paper.

Approximately 10-12 flask samples were captured during each flight. We screen data for overlapping high quality samples of CO_2, CO, and COS and fair-weather days (~50% of total samples, ranging from 32% in fall 2017 to 59% in summer 2019) using provided air mass flags (Wei et al., submitted). CO_2 samples collected during summer 2016 were replaced by continuous data from *in situ* systems on board both aircraft due to CO_2 depletion in undried flask air samples at water vapor levels above 1.7% (Baier et al., 2020). Moreover, nearly half of COS measurements analyzed during the first campaign failed to pass quality control criteria due to air sample contamination of COS measurements from o-rings, leading to reduced sample size in summer 2016 (52 flask samples) compared to subsequent campaigns (58-133). The total number of remaining samples per campaign ranges from 52-105 in the first three campaigns, and increases to 127 and 133 in the final two campaigns, respectively. In particular, we note a nearly factor of 3 increase in sample size from summer 2016 to summer 2019.

Aircraft tracks were designed to be within (~300 m AGL) or above the boundary layer (BL) as observed by on-board thermodynamics and lidar data. We focus on enhancements of tracer

concentrations within BL relative to background variability in order to maximize sensitivity to local-regional (~100-500 km) surface flux influences. We estimate BL enhancements as the difference between BL and free troposphere (FT) flask data as indicated by metadata flags (Wei et al., submitted). Baier et al (2020) show that FT data provides an effective measure of background conditions for CO_2 in winter. We provide additional simulation experiments using global atmospheric tracer simulations further justifying the use of FT data to define background conditions for all tracers and seasons studied here (*Text S1*). We denote BL enhancements (BL – FT) as ΔCO_2, ΔCO, and ΔCOS.

To estimate enhancements, we further sort data into BL and FT bins using provided flags, with BL data denoted by filled circles in Figure 1. The nature of this aircraft campaign is such that BL and FT data were not always collected in the same location. Rather, data were collected along level-altitude transects that were hundreds of kilometers long, and encompassed synoptic weather patterns, causing spatial disconnect between BL and FT samples. We therefore average all FT data collected in a single day to represent a mean background value per day. Specifically, for each day with at least one flask sample in the BL and FT, we take the mean value of all FT data, and subtract that from individual BL samples. By limiting the flight data to fair-weather conditions, we minimize large horizontal gradients associated for example with frontal boundaries (e.g., Baier et al 2020), increase the likelihood that the BL and FT data represent the same air mass, and minimize the potential for cloud convection to spread surface flux signatures into the FT.

2.2 Posterior Tracer Surface fluxes

In order to interpret the observed atmospheric tracer distributions, model atmospheric simulations are forced by surface fluxes of CO_2, COS, and CO. In this study, we aim to use a set of surface fluxes that are consistent with various observational data-streams. These surface fluxes are derived from a combination of "top-down" (i.e., posterior fluxes constrained by atmospheric data) and "bottom-up" (i.e., prior fluxes derived from land-surface models or ancillary data). For CO_2 and CO, we start with climatological "bottom-up" prior fluxes, and derive posterior fluxes using OCO-2 (for CO_2) and MOPITT (for CO). For COS, we explore three independent process-based and data-constrained estimates of plant COS uptake. The data and methods used to calculate these fluxes are summarized below.

206 **CO_2 Flux**

207 Net CO_2 flux is composed of the sum of net biosphere exchange (NBE, representing the sum of
208 net ecosystem exchange (NEE) + biomass burning), air-sea net CO_2 exchanges (Ocean), and
209 fossil fuel emissions. The net carbon balance and its constituent fluxes are derived from the
210 Carbon Monitoring System Flux (CMS-Flux) system (http://cmsflux.jpl.nasa.gov). The net or
211 "total" flux is constrained over the period 2015-2019 against column integrated CO_2 from OCO-
212 2 using a 4D-Var inversion system, based on the adjoint of the GEOS-Chem global transport
213 model at 4° x 5° degree spatial resolution (Liu et al, 2014; Liu et al., 2020b and references
214 therein). Over land, the posterior net carbon flux from CMS-Flux is attributed to NBE as it is the
215 largest source of variability in atmospheric CO2. The resulting posterior NBE adjusts the prior or
216 "bottom-up" NBE estimates from the CARDAMOM model-data fusion system, summarized in
217 Bloom et al (2016, 2020), which itself is constrained by multiple data streams including GOME-
218 2 SIF, MODIS Leaf Area Index, above-ground biomass, and soil carbon for NEE, and
219 FLUXCOM GPP and Global Fire Emissions Database version 4 (GFEDv4) for biomass burning.

220 Additional prior fluxes in CMS-Flux include ocean and fossil emissions summarized in Brix et al
221 (2015), Caroll et al (2020), and Oda et al (2018). In order to link these fluxes to aircraft
222 measurements, prior and posterior monthly fluxes are downscaled to 3-hour timescales for
223 diurnal footprint analysis of ACT-America samples (*Section 2.3*) using ERA-interim reanalysis
224 of global radiation and surface temperature, following the approach of Olson and Randerson
225 (2001).

226 **CO Flux**

227 Posterior CO fluxes in CMS-Flux are derived using a similar 4D-Var approach as is used for
228 CO_2 (Jiang et al., 2015; Kopacz et al., 2009, 2010), using CO observations from Measurements
229 of Pollution in the Troposphere (MOPITT) instrument. This approach is summarized in more
230 detail in Bowman et al. (2017) and Worden et al. (2019). Following Jiang et al. (2011), each
231 month is estimated independently with initial conditions supplied by a suboptimal Kalman filter
232 (Parrington et al., 2008). The configuration for the CO inversion follows Jiang et al. (2013)
233 where the control vector for CO emissions combines the combustion, biogenic, and methane CO
234 sources.

Prior CO flux components used in the inversion include combustion CO sources (fossil fuel, biofuel, and biomass burning), and CO oxidation from biogenic non-methane VOCs and methane. CO oxidation is assumed to be completed within the relatively coarse 4x5 scales and therefore are emitted at the surface. Precursor emissions of CO from biogenic sources are computed using the Model of Emissions of Gases and Aerosols from Nature (MEGAN) version 2.0 (Guenther et al., 2006). Biomass burning emissions are obtained from GFED4 (van der Werf et al., 2010). Anthropogenic emissions (fossil fuel and biofuel) combine off-line emission inventories from the Emission Database for Global Atmospheric Research global model (EDGAR v4.2; Olivier and Berdowski, 2001; 2012) and regional models over North America (Kuhns et al., 2003) propagating seasonal, weekly, and diurnal variation. Biogenic and biomass emissions are estimated at 3-hourly resolution, other fluxes are monthly.

COS Flux

We examine three independent process-based and data-constrained estimates of plant COS uptake from (1) the Simple Biosphere Model version 4 (SiB4) process model, (2) atmospheric data-constrained and independent geostatistical inverse modeling (GIM) framework, and (3) semi-empirical SIF-based constraint (GOPT). These products are described in more detail below. Other COS component fluxes prescribed in this study include soil uptake (Whelan et al., 2016), anthropogenic emissions (Kettle et al., 2002), and biomass burning (van der Werf et al., 2010). We note that SiB4 and GIM estimates are not year specific, and thus do not represent climate conditions at the time of ACT-America data collection.

SiB4

The Simple Biosphere Model (SiB4; Haynes et al., 2019a, 2019b) is a mechanistic and processed-based model that simulates land-atmosphere exchanges of energy, momentum and moisture, as well as the terrestrial carbon cycle. By simulating biogeochemical and biophysical processes over heterogeneous vegetation, SiB4 not only provides estimates of water, energy and carbon fluxes, but it also predicts a wide variety of land characteristics and properties, including soil moisture, soil carbon pools, biomass, leaf area index (LAI), albedo, COS, and SIF. To create a self-consistent, predictive model, SiB4 combines elements from a prognostic phenology model [SiBpp; Stöckli et al., 2008; Stöckli et al., 2011], a crop model [SiBcrop; Lokupitiya et al., 2009; Corbin et al., 2010], and a terrestrial carbon pool model [SiB-CASA; Schaefer et al., 2008;

Schaefer et al., 2009] into a single modeling framework. By combining the processes from these three previous versions of SiB and using tiles of plant functional types (PFTs) to represent land cover heterogeneity, we have created a model capable of investigating land surface properties and land-atmospheric exchanges on a variety of temporal and spatial scales.

Plant uptake of atmospheric CO_2 and COS are directly related to photosynthesis through diffusion by stomatal conductance and consumption by collocated reaction in the chloroplasts of leaves (Rubisco and carbonic anhydrase (CA), respectively) (Campbell et al., 2008; Berry et al., 2013). Diffusion of gases including CO_2, COS, and water vapor along the pathway from the atmosphere to leaf cell where biochemistry takes place is controlled by boundary layer, stomatal, and mesophyll conductance (Berry et al., 2013). The prognostic canopy air space in SiB4, and addition of mesophyll conductance scaling to Vcmax (and modulation by environmental conditions), enables direct calculations of plant COS uptake (Baker et al., 2003; Stockli and Vidale, 2005). We note that SiB4 also has its own representation of soil COS exchange, which is based on a respiration approach which assumes that more productive environments cause buildup of CA in the surface litter and near-surface soil, and thus respire more COS and as function of productivity (Berry et al., 2013). SiB4 based soil respiration of COS is used in place of Whelan-based soil exchange in the analysis of SiB4-based COS results.

GIM

Atmospheric trace gas applications of the geostatistical inverse modeling (GIM) framework have primarily been used to estimate surface net ecosystem exchange CO_2 fluxes (Michalak 2004) by coupling atmospheric trace gas observations to a model of atmospheric transport. The GIM framework allows for the incorporation of covariate datasets to help constrain the space-time patterns of surface flux estimates (Gourdji et al. 2008; Gourdji et al. 2012). The GIM approach used here optimizes plant COS fluxes over North America using COS observations from the NOAA airborne network (https://www.esrl.noaa.gov/gmd/ccgg/aircraft/) and remotely sensed SIF (GOME-2, Joiner et al. 2013) as a single covariate. SIF is used as a covariate to help the inversion capture the space time patterns of photosynthetic CO_2 and hence plant COS fluxes. This approach is based on a North American regional CO_2 inversion (Shiga et al 2018) using the same pre-computed footprint library created from the WRF-STILT atmospheric transport model (Nehrkorn et al. 2010) runs for NOAA's CarbonTracker Lagrange project

(https://www.esrl.noaa.gov/gmd/ccgg/carbontracker-lagrange/). The influence of the background is removed by subtracting the average of observations above 2.5 km in any given aircraft sampling profile from the observations in the lowest 1.5 km (boundary layer). To isolate plant COS fluxes, the influence from secondary COS fluxes from soils (Whelan et al. 2016), anthropogenic emissions (Zumkehr et al. 2018), and biomass burning (Stinecipher et al. 2019) have been removed by convolving these surface fluxes with the WRF-STILT footprints and then subtracting from the boundary layer observations. Plant COS fluxes are optimized yearly at 1x1 spatial resolution over North America from 2008-2012 using four different sets of covariance parameters assuming two different model-data mismatch variances and two different temporal correlation lengths (see Table S1). A 5-year climatology of the monthly average of these four inversion runs is used here to reduce the impact of both data gaps and the impact of covariance parameter choices.

GOPT

As mentioned above, plant uptake of atmospheric COS is directly related to photosynthesis through diffusion modulated by stomatal conductance. Even though most terrestrial biosphere models include a representation of stomatal conductance enabling prediction of GPP, and multiple empirical-based methods exist for constraining GPP against satellite vegetation data (Anav et al., 2015), most models don't simulate leaf COS uptake. To get around this limitation, we developed a simplified biome-specified linear regression method that converts GPP into COS plant uptake from the mechanism in the SIB4 model. Analysis of monthly mean plant COS and GPP output from SiB4 shows a biome-dependent linear relationship. Therefore, we compute the linear regressions from GPP to COS flux for broad MODIS-based biome classifications. We compute the slope 'k' and intercept 'b' in Equation 1 using SIB4's GPP and COS plant uptake data for each biome (ib).

$$\mathrm{COS}\,(x,y) = k\,(ib) \times \mathrm{GPP}\,(x,y) + b\,(ib) \qquad (1)$$

By applying the consistent biome specified regression model, we can derive COS plant uptake from any GPP product. Here, we derived SIF-based GPP estimates following Parazoo et al (2014), where year-specific monthly GPP at each grid point is inferred from a precision-weight minimization of spaceborne SIF, which is regressed against global GPP from upscaled flux tower data (e.g., Frankenberg et al., 2011; Jung et al., 2011) and subjected to prior knowledge of GPP

from an ensemble of terrestrial ecosystem models (Sitch et al., 2015). Their method is updated here using OCO-2 measured SIF constraints. Monthly GPP is downscaled to 3 hours using the same approach for NBE, and then used in equation 1 to estimate COS.

Total vs Biogenic Flux

Seasonal maps of posterior CO_2, CO, and COS flux (from GIM) are shown in Figure 2. The corresponding biogenic component is shown in Figure 3. For CO_2 and COS, total and biogenic fluxes show consistent magnitude and spatial distribution over the entire year. The main difference can be seen in the northeast and upper Midwest, where fossil fuel emissions are prevalent. Fossil emissions drive most of the COS flux and amplify CO_2 emissions in winter, and offset much of the plant-driven COS drawdown in summer. The CO posterior is driven largely by hotspots of emissions from fossil fuel (year-round) and fires in summer. Biogenic emissions occur mainly in summer in the south, lower Midwest, and along in the mid-Atlantic regions, and show consistent magnitude from early to late summer (June – August).

2.3 Atmospheric Signal Prediction

The preceding posterior fluxes are derived from atmospheric models run at fairly coarse spatial resolution. As such, when these fluxes are propagated back to the atmosphere using the same atmospheric models run in forward simulation mode, they will not capture the variability seen in the ACT-America samples. To bridge those scales, we run the HYbrid Single-Particle Lagrangian Integrated Trajectory (HYSPLIT) model (Draxler and Hess, 1997; Stein et al., 2015) in Stochastic Time-Inverted Lagrangian Transport (STILT)-emulation mode and driven by meteorological fields from the Weather Research and Forecasting Chemistry model (WRF-Chem; Feng et al., 2019a) to estimates surface influence (footprint) predictions for ACT-America flask samples.

The WRF-Chem simulation is carried out using version 3.6.1. The domain of interest contains most of North America [170°W - 60°W, 20°N – 75°N] at 27 km horizontal resolution. The model has 50 levels up to 50 hPa with 20 levels in the lowest 1 km. The model meteorology is initialized every 5 days and driven with ERA5 reanalysis every 6 hours at 25-km horizontal resolution. The WRF-Chem dynamic is relaxed to ERA5 (Hersbach et al, 2020) meteorology every 6 hours using grid nudging. Each meteorological re-initialization is started at a 12-hour setback from the end of the previous 5-day run. The first twelve hours of every 5-day simulation

354 are considered spin-up and discarded from the final analysis. We also update sea surface
355 temperature every 6 hours at 12-km resolution. Choices of the model physics parameterizations
356 used in this experiment are documented as the baseline setup described in Feng et al (2019a;
357 2019b). Specifically, MYNN 2.5 PBL scheme (Nakanishi and Niino, 2004) and Noah Land
358 surface model (Chen and Dudia, 2001) are used for vertical mixing.

359 WRF-HYSPLIT was run backward for 10 days, or until particles exit the North American
360 continental boundary, roughly defined by the WRF-Chem domain above. For each back
361 trajectory, 500 particles were released at each flask receptor location to generate footprints every
362 15 minutes along the particle trajectories. Surface footprints were re-calculated on a 1-degree
363 grid and saved at hourly intervals.

364 We note several differences in summer influence patterns in 2016 and 2019. The NE region
365 shows more local influence in 2016, and westerly and northerly influence in 2019. The MW
366 region has a larger southerly component in 2016. The S region is more southerly and easterly in
367 2016, and local/southerly in 2019. We also note a strong influence from the Gulf of Mexico in
368 both years.

369 **3. Results**

370 Observed seasonal tracer distribution in the BL and FT, and corresponding enhancements (Δ =
371 BL - FT), are shown in Figure S3 (top and bottom rows, respectively). Comparison to predicted
372 enhancements, determined by convolving prior and posterior surface fluxes with HYSPLIT
373 influence functions, is provided in Figure 5. We refer to $\Delta < 0$ (BL < FT) as depletion and $\Delta > 0$
374 (BL > FT) as enrichment. We also refer to CO production by biogenic VOCs as "biogenic CO
375 emission"

376 **3.1 Observed Tracer Seasonal Enhancements**

377 We point out several important features regarding seasonal amplitude and timing of observed
378 tracer variations, and seasonal covariance across tracers. In particular, ΔCO_2 drawdown is
379 consistently deeper and earlier in the BL compared to the FT across our three study regions,
380 leading to net depletion in early and late summer, and net enrichment in fall, winter and spring
381 (Figure S3). Focusing on BL enhancements, we note that the magnitude of peak ΔCO_2 depletion
382 roughly follows the north-south gradient, with deeper depletion in the NE and MW and

shallowest depletion in the S. The timing of peak depletion occurs in late summer in the NE, and early summer in MW and S. The seasonal and regional patterns are expected, but still encouraging given the inconsistent sampling of these regions in space and time.

ΔCOS shows positive seasonal correlation with ΔCO_2 in each region (r^2 = [0.48, 0.90]; see Table S2), including similar seasonal timing and magnitude. ΔCOS remains depleted on average in fall when ΔCO_2 becomes enriched, but the summer-to-fall tendency (reduced depletion) is in the same direction. Interestingly, peak ΔCO occurs in early and late summer in MW and NE, respectively, corresponding to peak ΔCOS and ΔCO_2 depletion, producing seasonal anti-correlation between ΔCOS-ΔCO and ΔCO_2-ΔCO in the MW and NE. Winter ΔCO enrichment in the MW and S is synchronized with peak ΔCO_2 enrichment, and negligible ΔCOS depletion.

3.2 Comparison of Observed and Simulated Seasonal Enhancements

Predicted signals from prior and posterior fluxes show surprisingly good agreement with observations in terms of seasonal timing, magnitude, and relative variability across tracers and regions (Figure 5 and Table S3). In most cases, predicted and observed tracer-tracer correlations have the same sign, including positive correlation of ΔCO_2-ΔCOS in all three regions, and negative correlation of ΔCO_2-ΔCO and ΔCOS-ΔCO in the NE and S regions. Similar seasonal and tracer-correlation patterns are found for prior and posterior flux estimates, with the following caveats: (1) significantly improved agreement in seasonal magnitude in ΔCO_2 posteriors (mean regression slope per region increases from 0.43 to 0.74; Table S3), (2) degraded seasonal amplitude but improved structure in the ΔCO posterior, and (3) regionally dependent performance in COS flux estimates. With these considerations, we can use the observationally-constrained model simulations to interpret seasonal and spatially variable biospheric influences on observed enhancement patterns, through comparison of posterior flux and surface influence maps (Figure 2-4) as discussed below.

We focus first on summer ΔCO_2 depletion in the NE region. The predominant surface influences occur within the Appalachian deciduous broadleaf forests, where posterior COS and CO_2 fluxes show regionally strong sinks, and CO flux shows a locally strong source. COS and CO_2 biogenic sinks are only slightly offset by anthropogenic emissions, while the CO source is persistent year-round but amplified by summer biogenic sources. The difference in timing of peak surface CO_2 uptake (early summer 2019) and peak ΔCO_2 depletion (late summer 2016) points to other

important influences besides the seasonal change in surface flux magnitude. In this case, we note a shift in the location and magnitude of the surface influence function, from a locally strong NE influence in late summer 2016, centered near a local sink hotspot in West Virginia, to a weaker westerly influence in early summer 2019. The shift in upstream influence is most likely driven by differences in predominant weather patterns on the sampling days and locations in 2016 vs 2019; other possible factors are discussed in more detail in *Section 4*.

Summer depletion in the MW region is driven by strong COS and CO_2 uptake across the Central Great Plains and into southern Canada. Enhanced depletion in summer 2019 is consistent with stronger influence over crop dominated landscapes in the upper Midwest. Screening flask data by geographic region of influence shows a decrease in the magnitude of ΔCO_2 and ΔCOS depletion on the two days with the strongest southerly influence (from -13 ppm to -5 ppm for ΔCO_2 and -80 ppt to -67 ppt for ΔCOS, on average). By contrast, these same days show a relative increase in ΔCO enrichment, aligned with a biogenic CO source along the Mississippi River in southern Arkansas (Figure 3). Likewise, reduced ΔCO_2 and ΔCOS depletion in summer 2016 (relative to summer 2019) is linked to a pattern of predominantly southerly influence in 15 of 19 flask samples. Screening for days with more northerly influence increases depletion of ΔCO_2 and ΔCOS (from -6 ppm to -11 ppm for ΔCO_2 and -39 ppt to -53 ppt for ΔCOS), and decreases ΔCO enrichment (from 18 ppb to 17 ppb). These results suggest a strong influence of crops and northern ecosystems on biogenic drawdown CO_2 and COS in the MW, a weak influence of crops on CO, and potential biogenic source of CO along the southern portion of the Mississippi River (which is overestimated in posterior estimates).

Flask data collected in the S region show a much stronger offshore surface and background influence compared to other regions. The reduced terrestrial influence compared to MW and NE regions partially explains the relatively weak magnitude of summer ΔCO_2 depletion. It's worth noting, however, increased ΔCOS depletion and ΔCO enrichment in summer 2016 (in the S), corresponding to increased influence from the southeast US where biogenic CO emissions and COS uptake are prevalent (but potentially underestimated in our prior and posterior models). We also find a strong local influence along the Mississippi river in summer 2019 where posterior CO emissions peak. This surface posterior CO source appears to have the same biogenic origin as

442 southerly influenced MW flask samples, and is most likely responsible for the predicted ΔCO
443 enrichment spike in summer 2019, which is overestimated compared to observations.

444 Observed ΔCO_2 enrichment in the NE region in winter is consistent with fossil emissions and
445 annually persistent CO emissions (Zumkehr et al., 2018). Observed and simulated ΔCO_2 show
446 diverging patterns in spring, with excessive depletion in predicted signals, indicative of excessive
447 prior and posterior biogenic uptake. We find similar patterns in the S and MW regions, with less
448 local fossil CO and COS influence (near Chicago) in spring.

449 **3.3 Tracer-tracer spatial correlations across individual BL flasks**

450 The analysis in *Section 3.2* focused on seasonally averaged tracers and their covariations,
451 providing an informative assessment of regionally and seasonally integrated fluxes. We are also
452 interested in how the spatial distribution of fluxes affects the correlation between individual flask
453 samples. For this, we examine the spatial covariance between tracers across individual flasks per
454 region and season, for observed and predicted enhancements. The results are plotted as seasonal
455 regression slopes in Figure 6, with values that are significant from zero and well correlated (R^2 >
456 0.25) denoted by symbols. An example regression for a single season and region is shown in
457 Figure 7 A-B. The number of BL samples per region ranges from 8 (S region, summer 2016) to
458 78 (NE region, summer 2019).

459 From an observational perspective, most regions and seasons show no significant spatial
460 covariation. However, we note several important covariations that facilitate our interpretation of
461 seasonal tracer depletion and enrichment. In particular, the S region shows persistent and
462 significant negative correlation between ΔCO_2-ΔCO and ΔCOS-ΔCO, and positive correlation
463 between ΔCO_2-ΔCO, from early summer through late fall. These patterns are consistent with
464 land-based biological depletion of ΔCO_2 (plant-driven ΔCOS and ΔCO_2 depletion increases with
465 ΔCO enrichment), but only lead to net regional ΔCO_2 depletion from early to late summer with
466 surface influences over the southern US (more discussion below). These tracer-tracer patterns
467 continue into fall, but are inconsistent with ΔCO_2 enrichment, and occur as surface influences
468 shift offshore, making inferences of a persistent southern biogenic CO_2 sink into fall
469 inconclusive.

470 Predicted enhancements from prior and posterior fluxes capture the negative ΔCOS-ΔCO
471 correlation in summer 2019, and increased regression slope in summer 2016, but underestimate

472 the slope of regression by a factor of two (Figure 6; -1.67 +/- 0.29 vs -0.852 +/- 0.14). Predicted
473 signals also underestimate the slope of ΔCO_2-ΔCOS regression by a factor of 3 (0.0675 +/- 0.026
474 vs .0265 +/- 0.018). The results suggest that models underestimate southern growing season CO_2
475 uptake, and ΔCO_2 depletion, due to weak photosynthetic drawdown upstream of flask samples.

476 We can investigate the effect of flux spatial variability on late summer ΔCOS-ΔCO correlation,
477 and subsequent model bias, in more detail through closer examination of individual flask
478 samples. Only three total days of campaign data were collected in summer 2016, with two days
479 (Aug 27-28) influenced primarily by the southeast US (easterly influence swath in Figure 4),
480 with high ΔCO and low ΔCOS air, and the other day (Aug 24) under more local to southerly
481 influence from Gulf inflow, with high ΔCOS and low ΔCO air (Figure 7A). It follows that the
482 observed ΔCOS-ΔCO negative correlation is driven in large part by covariance of CO precursor
483 emissions and COS uptake in the southeast US. As such, increasing the biogenic component of
484 posterior CO_2 (NBE) and COS (plant) uptake by factors of two each in the southeast region,
485 defined here as 90-80°W, 28-36°N, substantially improves the agreement between predicted and
486 observed tracer-tracer correlation patterns in the S region (Figure 7B). Regression slopes
487 increase by ~50% for ΔCOS-ΔCO (from -0.852 to -1.48 ppt / ppb), ~30% for ΔCO_2-ΔCOS (from
488 +0.0265 to +0.033 ppm / ppt), and ~300% for ΔCO_2-ΔCO (from -0.018 to -0.05 ppm / ppb). For
489 ΔCO_2-ΔCOS, we note that increasing the posterior biogenic COS flux alone actually degrades
490 the correlation, and that the combination of COS and CO_2 is needed (Figure 7H). The need for
491 increased COS and CO_2 uptake, and no change in CO, is consistent with seasonal comparisons
492 (Figure 6), which show that posteriors underestimate observed ΔCO_2 and ΔCOS depletions at
493 regional scale in late summer 2019. While a change in biogenic CO flux does not appear to be
494 necessary, we note that decreasing the biospheric CO emission by a factor of 2 further increases
495 the predicted ΔCOS-ΔCO slope by 20% (to -1.78 ppt / ppb) in much closer agreement with the
496 observed slope (Figure S4), demonstrating the important correlation of biogenic COS and CO
497 fluxes in the south. By contrast, reducing CO fossil emissions by half increases the ΔCOS-ΔCO
498 slope by 2%.

499 The ΔCOS-ΔCO correlation is further improved by considering salt marsh emissions as an
500 additional process not typically encountered in regional COS budgets. Salt marsh ecosystems are
501 a large emitters of COS. Instantaneous saline wetland emissions range from ~0 to 300 pmol m^{-2}

s^{-1} (Whelan et al., 2018). A surface flux campaign along the Texas shore of the Gulf of Mexico, within the footprint of Aug 24 ACT-America data analyzed here, estimated an average flux from vegetated plots of ~60 pmol m^{-2} s^{-1}, with larger values in July sometimes exceeding 110 pmol m^{-2} s^{-1} (Whelan et al., 2013). To assess the sensitivity of predicted ΔCOS-ΔCO correlations in the S region to salt marshes, we add salt marsh emissions to our total posterior COS flux by assuming a mean value of 70 pmol m^{-2} s^{-1} in July within gulf coast pixels and that vegetated salt marshes comprise ~200 km^2 of the Texas Gulf Coast in 2016 (extrapolating from Armatage et al., 2015). We note that the objective here is not to capture salt marshes exactly, but rather to provide a realistic estimate to demonstrate sensitivity of airborne tracer-tracer correlation patterns. Including salt marsh COS emissions increases the spatial gradient of COS fluxes, which acts on the spatial gradient of atmospheric signals in a small but non-trivial way, and increases the slope of regression of ΔCOS-ΔCO by 5%, from -1.48 to -1.55 (not shown).

4. Discussion

We analyzed boundary layer enhancements (BL – FT) of biologically-sensitive tracer species (CO_2, COS, CO) collected by ACT-America aircraft campaigns over four seasons and five campaigns from 2016-2019 against a corresponding set of independent, satellite-constrained surface fluxes to determine the spatial and seasonal influence of plant uptake on atmospheric CO_2 enhancements. We find a strong gradient of ΔCO_2 and ΔCOS drawdown from north to south, peaking in the northeast US in late summer, consistent with wider geographic region of influence in northern regions (eastern US + Canada) and limited upwind influence area in the S region. Our main result indicates a common terrestrial biogenic sink of CO_2 and COS and biogenic source of CO in summer spread mostly evenly throughout the eastern US, driven by uptake of CO_2 and COS by vegetation, and emission of biogenic VOCs, through stomatal conductance. In general, the magnitude, timing, and regional dependence of the summer CO_2 sink is well estimated by a CMS-Flux inversion system constrained by OCO-2 observed column CO_2, and represents a significant improvement over model-based estimates (based on increase in mean seasonal regression with observed values from 0.43 to 0.73).

We provide evidence that the magnitude of the terrestrial CO_2 sink, however, is underestimated by prior and satellite constrained models in the temperate humid forests in the southeast US. In particular, strong depletion of ΔCO_2 and ΔCOS and enrichment of ΔCO is observed in flask data

from August 27-28, 2016 in the southern US. The resulting significant negative regression between ΔCOS and ΔCO is underestimated by predicted signals, and requires a factor of two or more larger biogenic uptake than is estimated by CO_2 and COS inversion models.

Our main results are broadly consistent with findings from a similar study led by Hilton et al (2017), who benchmarked land surface estimates of COS uptake against airborne COS profiles, and found models with strong crop driven GPP uptake in the Midwest to be the most consistent with observations. However, we argue that this finding must be reframed in the context of unprecedented sampling of the southern US offered by ACT-America, and in particular the meteorological conditions during the two days from August 27-28, 2016 with surface influences originating in the southeast US, which otherwise have negligible influence on the findings here or in Hilton et al (2017). As such, regionally focused ACT-America flights suggest that GPP activity is driving summer CO_2 sinks throughout the eastern US, with the strongest sinks in the Midwest and Northeast regions, and stronger than expected sinks in the Southeast.

This also highlights a potential limitation in using spaceborne SIF to constrain GPP and COS together. While our SIF constrained COS models (GIM and OCO-2 SIF) capture the basic structure of the annual cycle, they do not capture the depth of growing season COS depletion in the Northeast and Southern regions with as much fidelity as in the Midwest. SIF provides a well-known indicator for GPP in crop regions which are typically irrigated and not subject to water stress, and can continue to photosynthesis in high light / high temperature conditions conducive to both increased SIF and stomatal conductance. As such, one possible implication is that SIF does not provide as accurate a measure of COS and/or GPP in the late growing season in temperate evergreen and deciduous forests in the South and Northeast, respectively, due to increased dissipation of light through other pathways such as sustained nonphotochemical quenching (e.g., Raczka et al 2019).

All three regions show observed net depletion of ΔCOS and enrichment of ΔCO_2 and ΔCO in Fall 2017, significantly so in the Northeast, which points to a GPP sink of COS and CO_2 in the fall but of insufficient magnitude to offset soil respiration and fossil fuel emissions (Baier et al., 2020). Moreover, all models underestimate fall ΔCOS depletion, and underestimate ΔCO_2 and ΔCO enrichment. While underestimated plant GPP uptake represents a common model culprit in the summer, it is unlikely to explain the divergent patterns of ΔCOS and ΔCO_2 in fall, the latter

of which would require larger compensating low biases in respiration and/or fossil emissions. We do note, however, systematic model underestimates of ΔCO_2 enrichment in winter and spring, when soils and plants are less active, suggesting that CO_2 respiration sources are underestimated. This points to the possibility of fossil emissions as the additional fall CO_2 source, and soils as a missing fall COS sink.

While seasonal tracer behavior follows expected patterns from seasonally variable biogenic sources, it also reflects year to year variability in weather, upstream surface influence, and climate. Our findings are based on the reconstructed seasonal cycle derived from five 6-week snapshots (winter, spring, early summer, late summer, fall) over a period of four years. We caution the reader about over-interpretation of our seasonal cycle as climatologically persistent features. Interannual variability in climate drivers, ecosystem response, emissions change, flask sampling frequency and location, atmospheric winds, background variability, and upstream surface influences can have strong impacts on observed variability within a given year, season, and weather system. For example, we note a factor of 3 fewer samples in the Northeast region in summer 2016 vs summer 2019, different surface influence regions between each campaign, extreme flooding in Louisiana in summer 2016 followed by a drought pattern in the south in 2016, which likely increased water limitation in plants in late summer, and extreme flooding in the Midwest in summer 2019 which delaying planting of crops (Yin et al., 2020). We also note that our background calculation, derived from limited data in the free troposphere, is subject to uncertainty especially in cases when BL and FT air do not share the same air mass. Except for the two days from August 27-28, 2016, the South region is influenced almost entirely by offshore background flow from the Gulf of Mexico. While unlikely, it is possible that conditions exist for which ΔCO_2 depletion is stronger in the South than in the Northeast, for example under a stably stratified atmosphere and more direct influence from the southeast US. While continuous observations of COS are a challenge, there exists a wealth of continuous *in situ* CO_2 data from ACT-America and surface towers in the Southeast (in Alabama and Mississippi) over the same period as the flask samples analyzed here (Miles et al., 2018). We recommend future efforts leveraging these data for more targeted study of surface influences from this critical region than is possible from our airborne based flask analysis.

Finally, while our predicted signals show high fidelity in capturing observed patterns of variability, we note several key model limitations. Satellite CO_2 and CO inversions are

constrained by column integrated observations, which are subject to spatially coherent and poorly constrained biases, and strongly dependent on transport models, which are subject to horizontal and vertical transport uncertainty (Parazoo et al., 2012; Schuh et al., 2020). Posterior fluxes are spatially coarse, ranging from 2° x 2.5° in the CO inversion model and 4° x 5° in CO_2 inversion model, making it difficult to separate anthropogenic emissions from biogenic fluxes in dense urban regions such as the Northeast, or separate land from ocean along the Gulf Coast. Future efforts should examine CT2019 North America 1° x 1° posterior fluxes for more detailed assessment of seasonal CO_2 uptake in the South region. We also note that top-down inversion estimates are derived as monthly means, and then temporally downscaled to daily resolution using solar radiation, and thus do not capture the true day-to-day variability as seen in the flask data. Additionally, our SIF-based estimates (GOPT) assume a linear relationship between SIF and GPP, and furthermore derive the relationship to COS using a linear model derived from SiB4 output. These estimates provide a realistic first guess, but more sophisticated SIF models accounting for non-photochemical quenching (e.g., Parazoo et al., 2020) are needed for accurate predictions of COS and GPP from observed SIF.

5. Conclusions

ACT-America airborne campaigns acquired vertically-resolved observations of biologically sensitive carbon species including CO_2, COS, and CO in flask samples, providing unprecedented insight into the seasonal and spatial distribution of carbon sinks across diverse bioclimatic regions in the eastern US. Our model-observation tracer-tracer analysis of boundary layer flask enhancements supports previous findings that biogenic CO_2 drawdown, and subsequent timing and magnitude of ΔCO_2 depletion, is spatially variable across the eastern US. Crops in the upper Midwest drive strong ΔCO_2 and ΔCOS depletion from early to late summer. Temperate forest in the Northeast drive strong ΔCO_2 and ΔCOS depletion in late summer. The unprecedented ACT-America flask samples uncovered evidence that humid temperate forests in the poorly constrained South continue to photosynthesize and absorb CO_2 and COS (and emit CO through biogenic VOC precursor emissions) deeper into the growing season than expected by model priors and posteriors. However, additional sampling in the South is needed to conclusively constrain the carbon dynamics of this under-sampled region. Predicted atmospheric signals based on satellite constrained inversion fluxes reproduce much of the observed seasonal and regional

623 variability, as well as variability across tracers, and indicate a stronger than expected sink of CO_2
624 in humid temperate forests in the southeast. Ongoing analysis of ACT-America data with respect
625 to independent satellite-constrained fluxes is needed to understand the impact of confounding
626 sources of variability in temporally sparse airborne acquisitions (e.g., interannual variability in
627 climate, transport, surface influence, and background flow), and refine missing carbon source
628 and sink processes.

629 **6. Data Availability**

630 ACT-America flask observations for all 5 airborne campaigns from 2016-2019 are archived at
631 ORNL (*https://doi.org/10.3334/ORNLDAAC/1593*). Prior and posterior surface fluxes for CO2
632 (NBE) are available at *https://cmsflux.jpl.nasa.gov/get-data/nbe-2020*. COS fluxes derived using
633 the GIM model are available as monthly average values from 2008-2012 at
634 *https://zenodo.org/record/4304602#.X8kSj6pKjIE*. HYSPLIT footprints used in the calculation
635 of predicted atmospheric tracer signals are currently available at
636 *ftp://aftp.cmdl.noaa.gov/pub/baier/*, but will move to
637 *ftp://aftp.cmdl.noaa.gov/products/carbontracker/lagrange/footprints/ACT/* during the review
638 process. Other surface fluxes including prior and posterior CO, and COS derived from the GOPT
639 method will be made available at *https://cmsflux.jpl.nasa.gov/*. Other datasets including COS
640 from SiB4, and assimilated atmospheric COS concentrations from the COS-OCS model (see
641 Supplemental) are currently available upon request, and will be archived during the review
642 process.

643 **7. Acknowledgements**

644 The Atmospheric Carbon and Transport (ACT) - America project is a NASA Earth Venture
645 Suborbital 2 project funded by NASA's Earth Science Division. Penn State investigators were
646 supported by NASA Grant NNX15AG76G. Bianca Baier acknowledges CIRES ACT grant
647 number NNX15AJ06G. We acknowledge Arlyn Andrews and Kirk Thoning for provision of
648 gridded HYSPLIT footprints in netCDF format, NOAA/GML laboratory personnel who have
649 conducted measurements of CO2/CO/COS in flasks for ACT flasks and network sites, and
650 especially Ben Miller for making COS measurements during ACT-America and conducting the
651 QA/QC on the contaminated flask samples. Maarten Krol is supported by funding from the
652 European Research Council (ERC) under the European Union's Horizon 2020 research and

innovation program under grant agreement No 742798 (http://cos-ocs.eu). This research was carried out at the Jet Propulsion Laboratory, California Institute of Technology, under a contract with the National Aeronautics and Space Administration (NASA).

8. References

Armitage AR, Highfield WE, Brody SD, Louchouarn P (2015) The Contribution of Mangrove Expansion to Salt Marsh Loss on the Texas Gulf Coast. PLoS ONE 10(5): e0125404. https://doi.org/10.1371/journal.pone.0125404

Arneth, A., Sitch, S., Pongratz, J., Stocker, B. D., Ciais, P., Poulter, B., … Zaehle, S. (2017). Historical carbon dioxide emissions caused by land-use changes are possibly larger than assumed. *Nature Geoscience*, *10*(2), 79–84. https://doi.org/10.1038/ngeo2882

Baier, B. C., Sweeney, C., Choi, Y., Davis, K. J., DiGangi, J. P., Feng, S., et al. (2020). Multispecies assessment of factors influencing regional CO2 and CH4 enhancements during the winter 2017 ACT-America campaign. Journal of Geophysical Research: Atmospheres, 125, e2019JD031339. https://doi.org/10.1029/2019JD031339

Baker, I., A. S. Denning, N. Hanan, L. Prihodko, M. Uliasz, P. L. Vidale, K. Davis, and P. Bakwin (2003), Simulated and observed fluxes of sensible and latent heat and CO2 at the WLEF-TV tower using SiB2.5, Global Change Biol., 9(9), 1262–1277.

Berry, J., Wolf, A., Campbell, J.E., Baker, I., Blake, N., Blake, D., Denning, A.S., Kawa, S.R., Montzka, S.A., Seibt, U. and Stimler, K., 2013. A coupled model of the global cycles of carbonyl sulfide and CO2: A possible new window on the carbon cycle. *Journal of Geophysical Research: Biogeosciences*, *118*(2), pp.842-852.

Bloom, A. A., Exbrayat, J.-F., van der Velde, I. R., Feng, L., & Williams, M. (2016). The decadal state of the terrestrial carbon cycle: Global retrievals of terrestrial carbon allocation, pools, and residence times. *Proceedings of the National Academy of Sciences*, *113*(5), 1285–1290. https://doi.org/10.1073/pnas.1515160113

Bloom, A. A., K. W. Bowman, J. Liu, A. G. Konings, J. R. Worden, **N. C. Parazoo** et al, Lagged effects dominate the inter-annua variability of the 2010-2015 tropical carbon balance, Biogeosciences., https://doi.org/10.5194/bg-2019-459, in review, 2020.

Bowman, K. W., Liu, J., Bloom, A. A., Parazoo, N. C., Lee, M., Jiang, Z., … Wunch, D. (2017). Global and Brazilian Carbon Response to El Niño Modoki 2011–2010. *Earth and Space Science*, *4*(10). https://doi.org/10.1002/2016EA000204

Brix, H., Menemenlis, D., Hill, C., Dutkiewicz, S., Jahn, O., Wang, D., … Zhang, H. (2015). Using Green's Functions to initialize and adjust a global, eddying ocean biogeochemistry general circulation model. Ocean Modelling, 95, 1–14. https://doi.org/10.1016/j.ocemod.2015.07.008

Byrne, B., Liu, J., Lee, M., Baker, I., Bowman, K. W., Deutscher, N. M., … Wunch, D. (2020a). Improved Constraints on Northern Extratropical CO2 Fluxes Obtained by Combining Surface-Based and Space-Based Atmospheric CO2 Measurements. *Journal of Geophysical Research: Atmospheres*, *125*(15). https://doi.org/10.1029/2019JD032029

Byrne, B., Liu, J., Bloom, A. A., Bowman, K. W., Butterfield, Z., Joiner, J., … Yin, Y. (2020b). Contrasting regional carbon cycle responses to seasonal climate anomalies across the east-west divide of temperate North America. *Global Biogeochemical Cycles*. https://doi.org/10.1029/2020gb006598

Campbell, J.E., Carmichael, G.R., Chai, T., Mena-Carrasco, M., Tang, Y., Blake, D.R., Blake, N.J., Vay, S.A., Collatz, G.J., Baker, I. and Berry, J.A., 2008. Photosynthetic control of atmospheric carbonyl sulfide during the growing season. *Science*, *322*(5904), pp.1085-1088.

Carroll, D., Menemenlis, D., Adkins, J.F., Bowman, K.W., Brix, H., Dutkiewicz, S., Fenty, I., Gierach, M.M., Hill, C., Jahn, O. and Landschützer, P., 2020. The ECCO-Darwin data-assimilative global ocean biogeochemistry model: Estimates of seasonal to multidecadal surface ocean pCO2 and air-sea CO2 flux. *Journal of Advances in Modeling Earth Systems*, *12*(10), p.e2019MS001888.

Chen, F. and Dudhia, J.: Coupling an Advanced Land Surface– Hydrology Model with the Penn State–NCAR MM5 Model- ing System. Part I: Model Implementation and Sensitivity, Mon. Weather Rev., 129, 569–585, 2001.

Corbin, K. D., A. S. Denning, E. Y. Lokupitiya, A.E. Schuh, K. J. Davis, N. Miles, S. Richardson, and I. T. Baker, 2010: Assessing the Impact of Crops on Regional CO_2 Fluxes and Atmospheric Concentrations. *Tellus*, 62B, 521-532.

Davis, K.J., M.D. Obland, B. Lin, T. Lauvaux, C. O'Dell, B. Meadows, E.V. Browell, J.P. DiGangi, C. Sweeney, M.J. McGill, J.D. Barrick, A.R. Nehrir, M.M. Yang, J.R. Bennett, B.C. Baier, A. Roiger, S. Pal, T. Gerken, A. Fried, S. Feng, R. Shrestha, M.A. Shook, G. Chen, L.J. Campbell, Z.R. Barkley, and R.M. Pauly. 2018. ACT-America: L3 Merged In Situ Atmospheric Trace Gases and Flask Data, Eastern USA. ORNL DAAC, Oak Ridge, Tennessee, USA. https://doi.org/10.3334/ORNLDAAC/1593

Davis, K.J., E.V. Browell, S. Feng, T. Lauvaux, M. Obland, S. Pal, B. Baier, D.F. Baker, I. Baker, Z.R. Barkley, K. Bowman, A.S. Denning, J.P. Digangi, J. Dobler, A. Fried, T. Gerken, K. Keller, B. Lin, A. Nehrir, C. O'Dell, L. Ott, A. Roiger, A. Schuh, Y. Wei, B. Weir, C. Williams, and M. Xue. Design and Implementation of the Atmospheric Carbon and Transport (ACT) – America Earth Venture Suborbital Mission, submitted to Earth and Space Sciences.

Draxler, R.R. and Hess, G.D., 1997. Description of the HYSPLIT4 modeling system.

Feng, S., T. Lauvaux, K. Klaus, K. Davis, P. Rayner, T. Oda, K. Gurney, 2019: A road map for improving the treatment of uncertainties in high-resolution regional carbon flux estimates. Geophys. Res. Lett., 46. https://doi.org/10.1029/2019GL082987

Feng, S., T. Lauvaux, K. Davis, K. Keller, Y. Zhou, C. Willimans, A. Schuh, J. Liu, I. Baker. Seasonal characteristics of model uncertainties from biogenic fluxes, transport, and large-scale boundary inflow in atmospheric CO2 simulations over North America, 2019. Journal of Geophysical Research: Atmospheres,124, 14,325–14,346, https://doi.org/10.1029/2019JD031165

Frankenberg, C., Fisher, J. B., Worden, J., Badgley, G., Saatchi, S. S., Lee, J., … Kuze, A. (2011). New global observations of the terrestrial carbon cycle from GOSAT: Patterns of plant fluorescence with gross primary productivity. *Geophysical Research Letters*, *38*(17).

733 Gourdji, S.M., Mueller, K.L., Schaefer, K. and Michalak, A.M. 2008. Global monthly averaged
734 CO_2 fluxes recovered using a geostatistical inverse modeling approach: 2. Results including
735 auxiliary environmental data. *Journal of Geophysical Research* 113(D21).

736 Gourdji, S.M., Mueller, K.L., Yadav, V., et al. 2012. North American CO_2 exchange: inter-
737 comparison of modeled estimates with results from a fine-scale atmospheric inversion.
738 *Biogeosciences* 9(1), pp. 457–475.

739 Guanter, L., Zhang, Y., Jung, M., Joiner, J., Voigt, M., Berry, J. A., … Griffis, T. J. (2014).
740 Global and time-resolved monitoring of crop photosynthesis with chlorophyll fluorescence.
741 *Proceedings of the National Academy of Sciences*, *111*(14), E1327–E1333.
742 https://doi.org/10.1073/pnas.1320008111

743 Guenther, A., Karl, T., Harley, P., Wiedinmyer, C., Palmer, P. I., and Geron, C.: Estimates of
744 global terrestrial isoprene emissions using MEGAN (Model of Emissions of Gases and Aerosols
745 from Nature), Atmos. Chem. Phys., 6, 3181–3210, doi:10.5194/acp-6- 3181-2006, 2006.

746 Guenther, A. B., Jiang, X., Heald, C. L., Sakulyanontvittaya, T., Duhl, T., Emmons, L. K., and
747 Wang, X.: The Model of Emissions of Gases and Aerosols from Nature version 2.1
748 (MEGAN2.1): an extended and updated framework for modeling biogenic emissions Geosci.
749 Model Dev., 5, 1471-1492, 2012.

750 Haynes, K.D., I.T. Baker, A.S. Denning, R. St¨ockli, K. Schaefer, E.Y. Lokupitiya, J.M. Haynes
751 (2019). Representing ecosystems using dynamic prognostic phenology based on biological
752 growth stages: Part 1. Implementation in the Simple Biosphere Model (SiB4). Accepted for
753 Pulication in J. Adv. Mod. Earth Sy.

754 Haynes, K.D., I.T. Baker, A.S. Denning, S. Wolf, G. Wohlfahrt, G. Kiely, R.C. Minaya (2019).
755 Representing ecosystems using dynamic prognostic phenology based on biological growth
756 stages: Part 2. Grassland carbon cycling. Accepted for Pulication in J. Adv. Mod. Earth Sy.

757 Hersbach, H., Bell, B., Berrisford, P., Hirahara, S., Horányi, A., Muñoz-Sabater, J., et al. (2020).
758 The ERA5 global reanalysis. Quarterly Journal of the Royal Meteorological Society, 146(730),
759 1999–2049. https://doi.org/10.1002/qj.3803

760 Hilton, T. W., Whelan, M. E., Zumkehr, A., Kulkarni, S., Berry, J. A., Baker, I. T., … Elliott
761 Campbell, J. (2017). Peak growing season gross uptake of carbon in North America is largest in
762 the Midwest USA. *Nature Climate Change*, *7*(6), 450–454. https://doi.org/10.1038/nclimate3272

763 Hilton, T. W. (2018). Photosynthesis in high definition. *Nature Climate Change*, *8*(1), 20–21.
764 https://doi.org/10.1038/s41558-017-0040-6

765 Hudman, R. C., Murray, L. T., Jacob, D. J., Millet, D. B., Turquety, S., Wu, S., … Sachse, G. W.
766 (2008). Biogenic versus anthropogenic sources of CO in the United States. *Geophysical*
767 *Research Letters*, *35*(4), 1–5. https://doi.org/10.1029/2007GL032393

768 Jiang, Z., Jones, D. B. A., Kopacz, M., Liu, J., Henze, D. K., & Heald, C. (2011). Quantifying
769 the impact of model errors on top-down estimates of carbon monoxide emissions using satellite
770 observations. Journal of Geophysical Research, 116, D15306.
771 https://doi.org/10.1029/2010JD015282

772 Jiang, Z., Jones, D. B. A., Worden, H. M., Deeter, M. N., Henze, D. K., Worden, J., … Schuck,
773 T. J. (2013). Impact of model errors in convective transport on CO source estimates inferred

from MOPITT CO retrievals. Journal of Geophysical Research: Atmospheres, 118, 2073–2083. https://doi.org/10.1002/jgrd.50216

Jiang, Z., Worden, J. R., Jones, D. B. A., Lin, J. T., Verstraeten, W. W., & Henze, D. K. (2015). Constraints on Asian ozone using Aura TES, OMI and Terra MOPITT. Atmospheric Chemistry and Physics, 15(1), 99–112. https://doi.org/10.5194/acp-15-99-2015

Joiner, J., Guanter, L., Lindstrot, R., et al. 2013. Global monitoring of terrestrial chlorophyll fluorescence from moderate-spectral-resolution near-infrared satellite measurements: methodology, simulations, and application to GOME-2. *Atmospheric measurement techniques* 6(10), pp. 2803–2823.

Jung, M., Reichstein, M., Margolis, H. A., Cescatti, A., Richardson, A. D., Arain, M. A., … Williams, C. (2011). Global patterns of land-atmosphere fluxes of carbon dioxide, latent heat, and sensible heat derived from eddy covariance, satellite, and meteorological observations. *Journal of Geophysical Research: Biogeosciences*, *116*(3), 1–16. https://doi.org/10.1029/2010JG001566

Kettle, A. J., Kuhn, U., von Hobe, M., Kesselmeier, J. & Andreae, M. O. Global budget of atmospheric carbonyl sulfide: temporal and spatial variations of the dominant sources and sinks. J. Geophys. Res. 107, (2002).

Kopacz, M., Jacob, D. J., Henze, D. K., Heald, C. L., Streets, D. G., & Zhang, Q. (2009). Comparison of adjoint and analytical Bayesian inversion methods for constraining Asian sources of carbon monoxide using satellite (MOPITT) measurements of CO columns. Journal of Geophysical Research, 114, D04305. https://doi.org/10.1029/2007JD009264

Kopacz, M. et al. Global estimates of CO sources with high resolution by adjoint inversion of multiple satellite datasets (MOPITT, AIRS, SCIAMACHY, TES). Atmos. Chem. Phys. 10, 855–876 (2010).

Kuhns, H., Green, M., and Etyemezian, V.: Big Bend Regional Aerosol and Visibility Observational (BRAVO) Study Emissions Inventory, Report prepared for BRAVO Steering Committee, Desert Research Institute, Las Vegas, Nevada, 2003.

Liu, J., Bowman, K., Lee, M., Henze, D., Bousserez, N., Brix, H., … Nassar, R. (2014). Carbon monitoring system flux estimation and attribution: impact of ACOS-GOSAT XCO2 sampling on the inference of terrestrial biospheric sources and sinks. Tellus B, 66, 22486. https://doi.org/10.3402/tellusb.v66.22486

Liu, J., & Wennberg, P. O. (2020a). Observational Constraints on the Response of High - Latitude Northern Forests to Warming.

Liu, J., Baskaran, L., Bowman, K., Schimel, D., Bloom, A.A., Parazoo, N.C., Oda, T., Carroll, D., Menemenlis, D., Joiner, J. and Commane, R., 2020b. Carbon Monitoring System Flux Net Biosphere Exchange 2020 (CMS-Flux NBE 2020). *Earth System Science Data Discussions*, pp.1-53.

Lokupitiya E., S. Denning, K. Paustian, I. Baker, K. Schaefer, S. Verma, T. Meyers, C.J. Bernacchi, A. Suyker, M. Fischer (2009). Incorporation of Crop Phenology in Simple Biosphere Model (SiBcrop) to Improve Land-Atmosphere Carbon Exchanges from Croplands. *Biogeosci*., 6, 969-986

Madani, N., N. C. Parazoo, J. S. Kimball, A. P. Ballantyne, S. Saatchi, P. I. Palmer, Z. Liu, T. Tagesson, A. Bloom, Amplified global gross primary productivity due to temperature increase is offset by reduced productivity due to water constraint, AGU Advances, In Press

Michalak, A.M. 2004. A geostatistical approach to surface flux estimation of atmospheric trace gases. *Journal of Geophysical Research* 109(D14).

Miles, N. L., S. J. Richardson, K. J. Davis, T. Lauvaux, A. E. Andrews, T. O. West, V. Bandaru, and E. R. Crosson, 2012. Large amplitude spatial and temporal gradients in atmospheric boundary layer CO2 mole fractions detected with a tower-based network in the U.S. upper Midwest, J. Geophys. Res., **117**, G01019, doi:10.1029/2011JG001781.

Miles, N.L., S.J. Richardson, D.K. Martins, K.J. Davis, T. Lauvaux, B.J. Haupt, and S.K. Miller. 2018. ACT-America: L2 In Situ CO2, CO, and CH4 Concentrations from Towers, Eastern USA. ORNL DAAC, Oak Ridge, Tennessee, USA. https://doi.org/10.3334/ORNLDAAC/1568

Nakanishi, M. and Niino, H.: An improved Mellor-Yamada Level-3 model with condensation physics: Its design and verification, Bound.-Lay. Meteorol., 112, 1–31, https://doi.org/10.1023/B:BOUN.0000020164.04146.98, 2004.

Nehrkorn, T., Eluszkiewicz, J., Wofsy, S.C., et al. 2010. Coupled weather research and forecasting–stochastic time-inverted lagrangian transport (WRF–STILT) model. *Meteorology and Atmospheric Physics* 107(1–2), pp. 51–64.

Oda, T., Maksyutov, S. and Andres, R.J., 2018. The Open-source Data Inventory for Anthropogenic Carbon dioxide (CO2), version 2016 (ODIAC2016): A global, monthly fossil-fuel CO2 gridded emission data product for tracer transport simulations and surface flux inversions. *Earth system science data*, *10*(1), p.87.

Olivier, J. G. J. and Berdowski, J. J. M.: Global emissions sources and sinks, in: The Climate System, edited by: Berdowski, J., Guicherit, R., and Heij, B. J., A. A. Balkema Publishers/Swets & Zeitlinger Publishers, Lisse, the Netherlands, 33–78, 2001.

Olsen, S. C., & Randerson, J. T. (2004). Differences between surface and column atmospheric CO2 and implications for carbon cycle research, Journal of Geophysical Research, 109, D02301. https://doi.org/10.1029/ 2003JD003968

Parazoo, N. C., A. S. Denning, S. R. Kawa, S. Pawson, and R. Lokupitiya, 2012: CO_2 flux estimation errors associated with moist atmospheric processes, *Atmos. Chem. Phys.*, 12, 6405-6416.

Parazoo, N. C., Bowman, K., Fisher, J. B., Frankenberg, C., Jones, D. B. A., Cescatti, A., … Montagnani, L. (2014). Terrestrial gross primary production inferred from satellite fluorescence and vegetation models. *Global Change Biology*, *20*(10). https://doi.org/10.1111/gcb.12652

Parazoo, N. C., Commane, R., Wofsy, S. C., Koven, C. D., Sweeney, C., Lawrence, D. M., … Miller, C. E. (2016). Detecting regional patterns of changing CO2 flux in Alaska. *Proceedings of the National Academy of Sciences of the United States of America*, *113*(28). https://doi.org/10.1073/pnas.1601085113

Parazoo, N. C., T. Magney, I Baker, B Raczka, C Bacour, F Maignan, A Norton, Y Zhang, M Shi, N MacBean, D. R. Bowling, S. P. Burns, P. D. Blanken, J. Stutz, K Grossman, C Frankenberg, 2020: Wide Discrepancies in the Magnitude and Direction of Modelled SIF in

Response to Light Conditions, Biogeosciences, 17 (13), 3733-3755, https://doi.org/10.5194/bg-17-3733-2020.

Parrington, M., Jones, D. B. A., Bowman, K. W., Horowitz, L. W., Thompson, A. M., Tarasick, D. W., & Witte, J. C. (2008). Estimating the summertime tropospheric ozone distribution over North America through assimilation of observations from the tropospheric emission spectrometer. Journal of Geophysical Research, 113, D18307. https://doi.org/10.1029/2007JD009341

Peters, W., Jacobson, A. R., Sweeney, C., Andrews, A. E., Conway, T. J., Masarie, K., … Tans, P. P. (2007). An atmospheric perspective on North American carbon dioxide exchange: CarbonTracker. *Proceedings of the National Academy of Sciences of the United States of America*, *104*(48), 18925–18930. https://doi.org/10.1073/pnas.0708986104

Raczka, B., Porcar-Castell, A., Magney, T., Lee, J. E., Köhler, P., Frankenberg, C., … Bowling, D. R. (2019). Sustained Nonphotochemical Quenching Shapes the Seasonal Pattern of Solar-Induced Fluorescence at a High-Elevation Evergreen Forest. *Journal of Geophysical Research: Biogeosciences*, *124*(7), 2005–2020. https://doi.org/10.1029/2018JG004883

Schaefer K., T. Zhang, A.G. Slater, L. Lu, A. Etringer, I. Baker (2009). Improving Simulated Soil Temperatures and Soil Freeze/Thaw at High-Latitude Regions in Simple Biosphere/ Carnegie-Ames-Stanford Approach Model. *J. Geophys. Res.,* 114 (F02021), doi:10.1029/2008JF001125.

Schaefer K., G.J. Collatz, P. Tans, A.S. Denning, I. Baker, J. Berry, L. Prihodko, N. Suits, A. Philpott (2008). Combined Simple Biosphere/Carnegie-Ames-Stanford Approach Terrestrial Carbon Cycle Model. *J. Geophys. Res*., 113 (G03034), doi:10.1029/2007JG000603.

Schuh, Andrew E., Thomas Lauvaux, Tris West, A. Scott Denning, Kenneth J. Davis, Natasha Miles, Scott Richardson, Marek Uliasz, Erandathie Lokupitiya, Daniel Cooley, Arlyn Andrews, and Stephen Ogle, 2013. Evaluating atmospheric CO_2 inversions at multiple scales over a highly-inventoried agricultural landscape. Global Change Biology. **9**, 1424-1439, doi: 10.1111/gcb.12141

Schuh, A.E., Jacobson, A.R., Basu, S., Weir, B., Baker, D., Bowman, K., Chevallier, F., Crowell, S., Davis, K.J., Deng, F. and Denning, S., 2019. Quantifying the impact of atmospheric transport uncertainty on CO2 surface flux estimates. *Global biogeochemical cycles*, *33*(4), pp.484-500.

Schimel, D., Stephens, B. B., & Fisher, J. B. (2015). Effect of increasing CO_2 on the terrestrial carbon cycle. *Proceedings of the National Academy of Sciences*, *112*(2), 436–441. https://doi.org/10.1073/pnas.1407302112

Shiga, Y.P., Tadić, J.M., Qiu, X., Yadav, V., Andrews, A.E., Berry, J.A. and Michalak, A.M., 2018. Atmospheric CO2 observations reveal strong correlation between regional net biospheric carbon uptake and solar-induced chlorophyll fluorescence. *Geophysical Research Letters*, *45*(2), pp.1122-1132.

Sitch, S., Friedlingstein, P., Gruber, N., Jones, S. D., Murray-Tortarolo, G., Ahlström, A., … Myneni, R. (2015). Recent trends and drivers of regional sources and sinks of carbon dioxide. *Biogeosciences*, *12*(3), 653–679. https://doi.org/10.5194/bg-12-653-2015

Stein, A.F., Draxler, R.R., Rolph, G.D., Stunder, B.J., Cohen, M.D. and Ngan, F., 2015. NOAA's HYSPLIT atmospheric transport and dispersion modeling system. *Bulletin of the American Meteorological Society*, *96*(12), pp.2059-2077.

Stephens, B. B., Gurney, K. R., Tans, P. P., Sweeney, C., Peters, W., Bruhwiler, L., … Denning, A. S. (2007). Weak northern and strong tropical land carbon uptake from vertical profiles of atmospheric CO2. *Science*, *316*(5832), 1732–1735. https://doi.org/10.1126/science.1137004

Stinecipher, J.R., Cameron-Smith, P.J., Blake, N.J., et al. 2019. Biomass burning unlikely to account for missing source of carbonyl sulfide. *Geophysical Research Letters* 46(24), pp. 14912–14920.

Stöckli, R. and Vidale, P.L., 2005. Modeling diurnal to seasonal water and heat exchanges at European Fluxnet sites. *Theoretical and applied climatology*, *80*(2-4), pp.229-243.

Stöckli, R., D. M. Lawrence, G.-Y. Niu, K. W. Oleson, P. E. Thornton, Z. L. Yang, G. B. Bonan, S. Denning, and S. W. Running (2008a), Use of FLUXNET in the Community Land Model development, *J. Geophys. Res.*, *113*(G1), doi:10.1029/2007JG000562.

Stöckli, R., T. Rutishauser, D. Dragoni, J. O'Keefe, P. E. Thornton, M. Jolly, L. Lu, and S. Denning (2008b), Remote sensing data assimilation for a prognostic phenology model, *J. Geophys. Res.*, *113*(G4), G04021, doi:10.1029/2008JG000781.

Sweeney, C., Karion, A., Wolter, S., Newberger, T., Guenther, D., Higgs, J.A., Andrews, A.E., Lang, P.M., Neff, D., Dlugokencky, E. and Miller, J.B., 2015. Seasonal climatology of CO2 across North America from aircraft measurements in the NOAA/ESRL Global Greenhouse Gas Reference Network. *Journal of Geophysical Research: Atmospheres*, *120*(10), pp.5155-5190

van der Werf, G. R., Randerson, J. T., Giglio, L., Collatz, G. J., Mu, M., Kasibhatla, P. S., Morton, D. C., DeFries, R. S., Jin,Y., and van Leeuwen, T. T.: Global fire emissions and the contribution of deforestation, savanna, forest, agricultural, and peat fires (1997– 2009), Atmos. Chem. Phys., 10, 11707–11735, doi:10.5194/acp- 10-11707-2010, 2010.

van der Werf, G. R. et al. Global fire emissions estimates during 1997–2016. Earth Syst. Sci. Data 9, 697-720 (2017).

Wei, Y., R. Shrestha, S. Pal, T. Gerken, J. McNelis, D. Singh, M.M. Thornton, A.G. Boyer, M.A. Shook, G.Chen, B.C. Baier, Z.R. Barkley, J.D. Barrick, J.R. Bennett, E.V. Browell, J.F. Campbell, L.J. Campbell, Y. Choi, J. Collins, J. Dobler, M. Eckl, S. Feng, A. Fiehn, A. Fried, J.P. Digangi, R. Barton-Grimley, H. Halliday, T. Klausner, S. Kooi, J. Kostinek, T. Lauvaux, B. Lin, M. McGill, B. Meadows, N.L. Miles, A.R. Nehrir, J.B. Nowak, M. Obland, C. O'Dell, R.M.P. Fao, S.J. Richardson, D. Richter, A. Roiger, C. Sweeney, J. Walega, P. Weibring, C.A. Williams, M.M. Yang, Y. Zhou, & K.J. Davis. The Atmospheric Carbon and Transport (ACT) – America Datasets: Description, Management, and Delivery. submitted to Earth and Space Sciences.

Whelan, M.E., Hilton, T.W., Berry, J.A., Berkelhammer, M., Desai, A.R. and Campbell, J.E. 2016. Carbonyl sulfide exchange in soils for better estimates of ecosystem carbon uptake. *Atmospheric Chemistry and Physics* 16(6), pp. 3711–3726.

Whelan, M. E., Anderegg, L. D. L., Badgley, G., Campbell, J. E., Commane, R., Frankenberg, C., … Worden, J. (2020). Scientific Communities Striving for a Common Cause: Innovations in

Carbon Cycle Science. *Bulletin of the American Meteorological Society*, *101*(9), E1537–E1543. https://doi.org/10.1175/bams-d-19-0306.1

Worden, H. M., Bloom, A. A., Worden, J. R., Jiang, Z., Marais, E. A., Stavrakou, T., Gaubert, B., and Lacey, F.: New constraints on biogenic emissions using satellite-based estimates of carbon monoxide fluxes, Atmos. Chem. Phys., 19, 13569–13579, https://doi.org/10.5194/acp-19-13569-2019, 2019.

Yin, Y., Byrne, B., Liu, J., Wennberg, P., Davis, K. J., Magney, T., et al. (2020). Cropland carbon uptake delayed and reduced by 2019 Midwest floods. AGU Advances, 1, e2019AV000140. https://doi.org/10.1029/2019AV000140

Zumkehr, A., Hilton, T.W., Whelan, M., et al. 2018. Global gridded anthropogenic emissions inventory of carbonyl sulfide. *Atmospheric environment* 183, pp. 11–19.

Figure Captions

Figure 1. Total remaining Portable Flask Package (PFP) samples per campaign after screening for fair weather days and overlapping high quality CO_2, COS, and CO data. Samples are color coded by region (Red = Midwest (MW), Green = South (S), Blue = Northeast (NE)). Filled circles denote boundary layer samples (altitude < 2 km agl).

Figure 2. Posterior surface fluxes of CO_2, CO, and COS corresponding to the five ACT-America campaigns from 2016-2019. Flux maps are time-resolved (1-3 hour) but plotted here as the two-month average over each campaign period in order of season and month(s) of year. Posterior fluxes are constrained by satellite observations using global top-down inversion methods for CO_2 and CO, and bottom-up geostatistical inversion methods for COS (GIM). Prior fluxes from which posterior fluxes are derived are not shown, but exhibit similar spatial patterns which are scaled up or down using inverse methods. Surface fluxes of COS derived using the SIB4 model and OCO-2 SIF constraints (GOPT) are not shown. Time resolved fluxes are then convolved with 10-day HYSPLIT footprints for each flask sample, which are shown in Figure 4.

Figure 3. Same as Fig 2, but for plant component of total flux.

Figure 4. Concentration footprints corresponding to boundary layer flask data collected during five ACT campaigns. Footprints are organized by campaign (columns, in order of season and month(s) of year) and flask sampling region (Northeast in top row; South in middle row; Midwest in bottom row). Footprints for Footprints are derived for each flask sample using surface influence functions from the HYSPLIT langrangian back-trajectory model, and convolved with time resolved prior and posterior fluxes to determine predicted signals for comparison with observed signals. Footprints shown here represent a data-collection time average, with footprints from individual samples summed over the previous 10 days, and then averaged across all samples within each region for each campaign.

Figure 5. Observed and satellite constrained (prior and posterior) seasonal tracer enhancement (Δ = FT – BL), separated by region (columns). Observed enhancements as in Figure S3. Satellite constrained fluxes are convolved with WRF-STILT footprints to determine atmospheric concentrations at ACT flask samples. Prior fluxes are derived from a range of natural and anthropogenic model and inventory estimates (see main text). Posterior CO_2 fluxes (top row) are

constrained by OCO-2 CO_2. COS fluxes are derived from SiB4, the GIM geostatisical inversion, and OCO-2 SIF linear regression model. Posterior CO derived from MOPITT CO.

Figure 6. Multi-tracer spatial regression. Each point represents the slope of the spatial regression between tracer enhancements across all boundary layer samples within a single season and region, including ΔCO_2 and ΔCO (top row), ΔCO_2 and ΔCOS (middle row), and ΔCOS and ΔCO (bottom row). Observed regressions are shown in black, simulated regressions in color, and regions are color coded. Markers represent points with statistically significant regressions (slope significantly different from zero, $r^2 > 0.25$). Simulated regressions are based on prior (dotted) and posterior (dashed fluxes). Only results for SIB4 (dotted) and GIM (dashed) are shown for ΔCOS regressions.

Figure 7. Surface flux drivers of observed tracer-tracer correlations in ACT-America South region in Summer 2016. (A,E,I) Observed ΔCO and ΔCOS mole fractions show distinct spatial gradients, with lower ΔCO / higher ΔCOS to the southwest (Aug 24, 2016) and higher ΔCO / lower ΔCOS to the northeast (Aug 27-28, 2016). (B-J) Observed and simulated tracer-tracer regression slopes for ΔCOS-ΔCO (top), ΔCO_2-ΔCOS (middle), and ΔCO_2-ΔCO (bottom). (B,F,J) Observed regressions, (C,G,K) Posterior regressions, (D,H,L) Posterior regressions based on perturbed fluxes of ΔCOS and ΔCO_2, determined by multiplying biogenic flux components within the southern region (90°W-80°W, 28°N-36°N) by a factor of 2 (denoted by * in title).

Campaign 1: Summer 2016

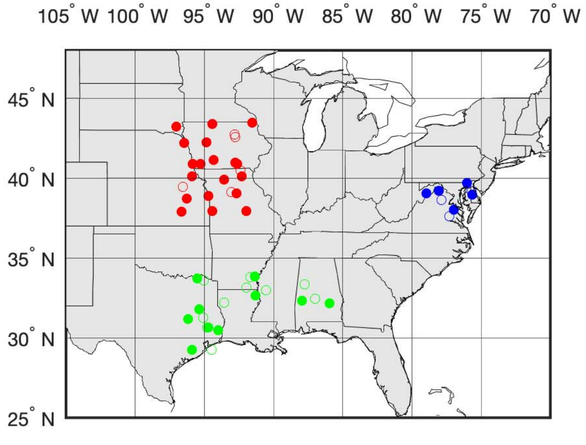

Campaign 2: Winter 2017

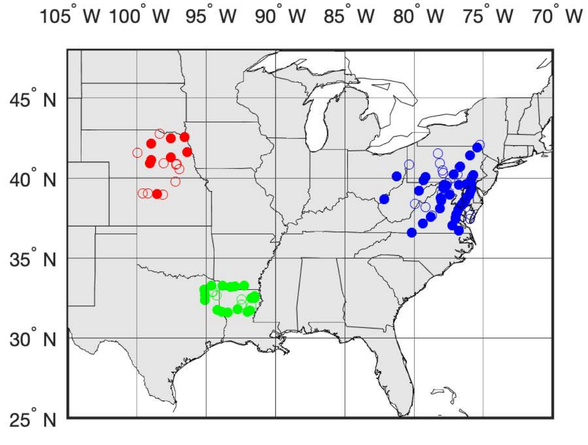

Campaign 3: Fall 2017

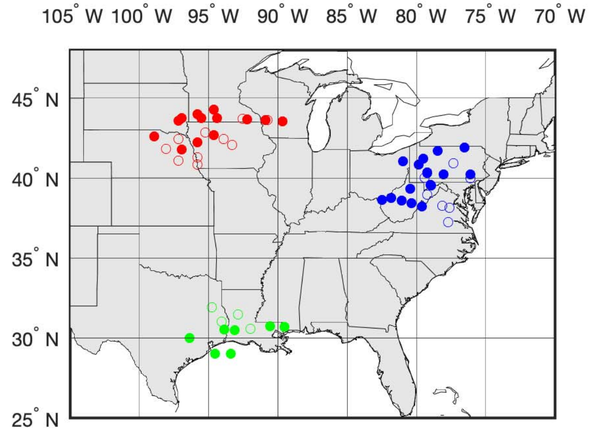

Campaign 4: Spring 2018

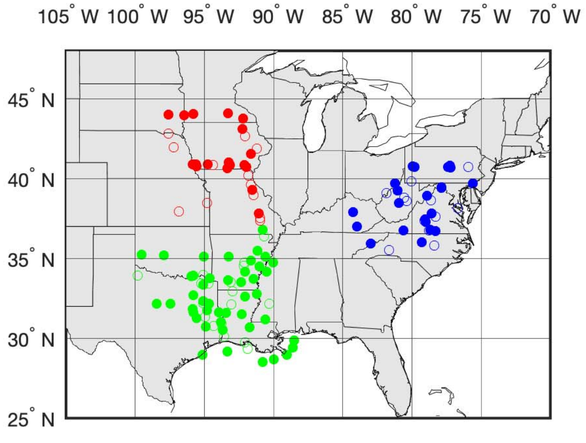

Campaign 5: Summer 2019

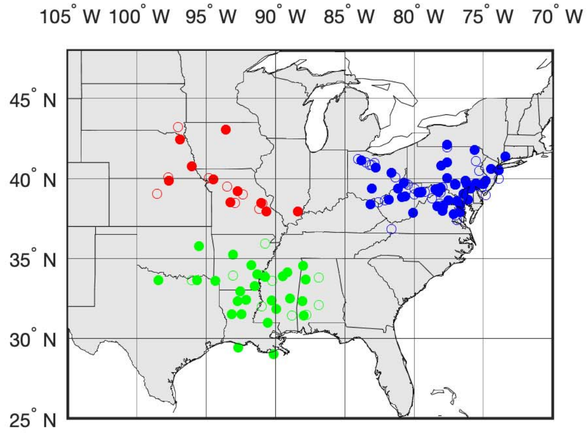

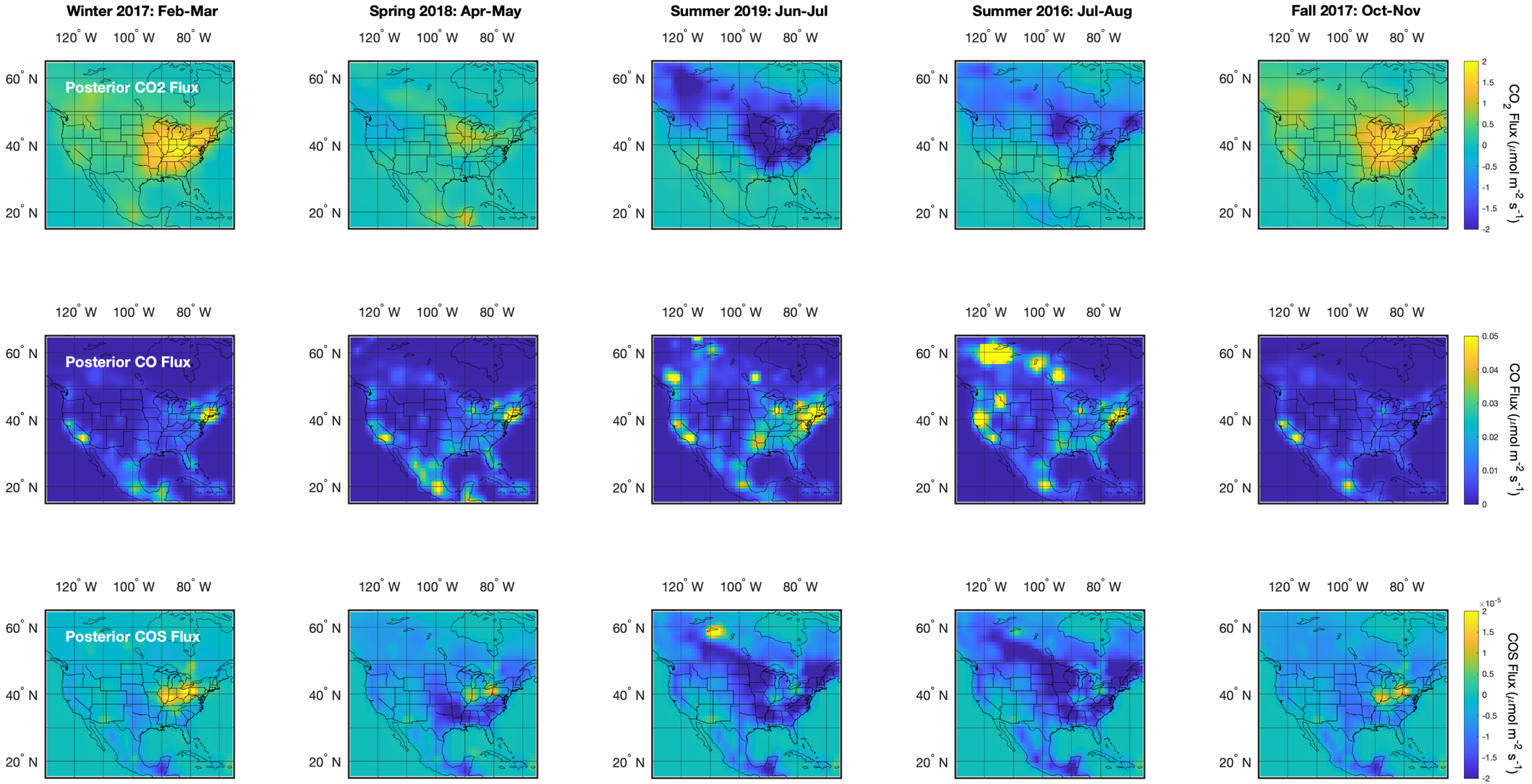
Winter 2017: Feb-Mar
Spring 2018: Apr-May
Summer 2019: Jun-Jul
Summer 2016: Jul-Aug
Fall 2017: Oct-Nov
Posterior CO2 Flux
Posterior CO Flux
Posterior COS Flux
120° W
100° W
80° W
60° N
40° N
20° N
CO2 Flux (μmol m-2 s-1)
CO Flux (μmol m-2 s-1)
COS Flux (μmol m-2 s-1)
×10-5

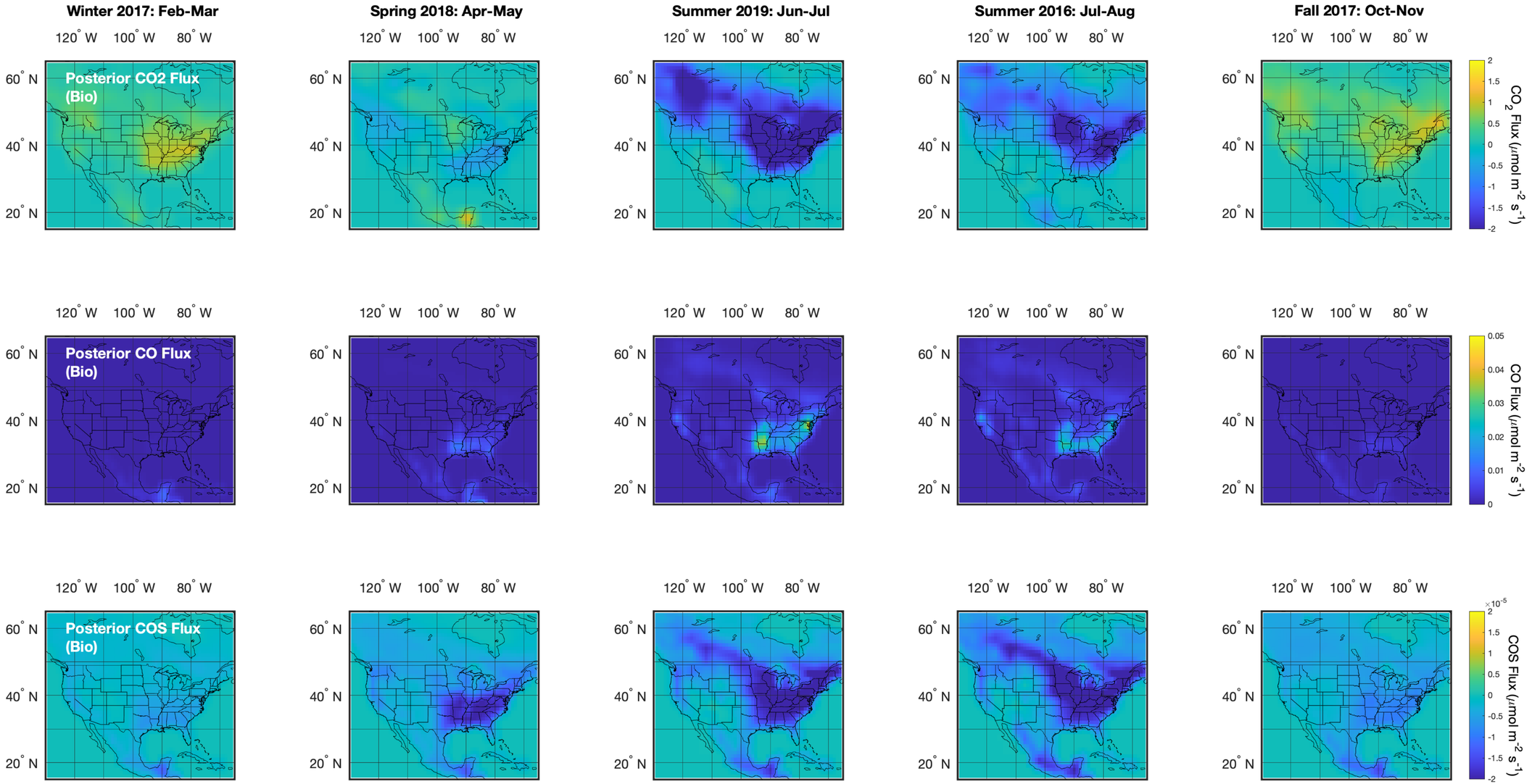
Winter 2017: Feb-Mar
Spring 2018: Apr-May
Summer 2019: Jun-Jul
Summer 2016: Jul-Aug
Fall 2017: Oct-Nov
Posterior CO2 Flux (Bio)
Posterior CO Flux (Bio)
Posterior COS Flux (Bio)
120° W
100° W
80° W
60° N
40° N
20° N
CO2 Flux (μmol m-2 s-1)
CO Flux (μmol m-2 s-1)
COS Flux (μmol m-2 s-1)
×10-5

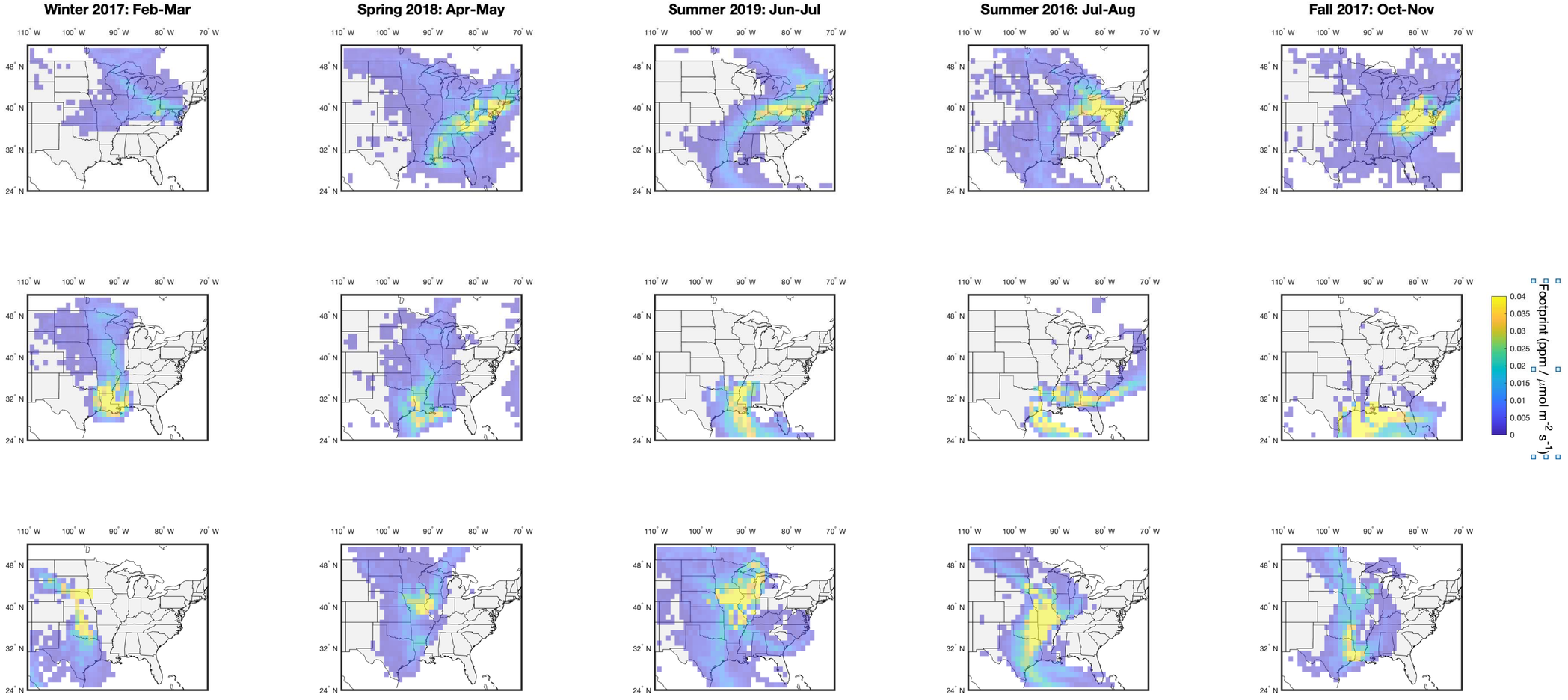
Winter 2017: Feb-Mar
Spring 2018: Apr-May
Summer 2019: Jun-Jul
Summer 2016: Jul-Aug
Fall 2017: Oct-Nov
110° W
100° W
90° W
80° W
70° W
48° N
40° N
32° N
24° N
Footprint (ppm / μmol m-2 s-1)
0.04
0.035
0.03
0.025
0.02
0.015
0.01
0.005
0

Northeast (NE)

South (S)

Midwest (MW)

ΔCO_2 (ppm)

10 5 0 -5 -10 -15 -20

Win Spr Sum19 Sum16 Fal

Observed
Prior
Posterior: OCO-2 CO2

ΔCO (ppb)

150 100 50 0

Win Spr Sum19 Sum16 Fal

Observed
Prior
Posterior: MOPITT CO

ΔCOS (ppt)

20 0 -20 -40 -60 -80 -100 -120

Win Spr Sum19 Sum16 Fal

Observed
Prior: SIB4
Posterior: GIM
Posterior: OCO-2 SIF

Regression Slope Between ΔCO_2 and ΔCO

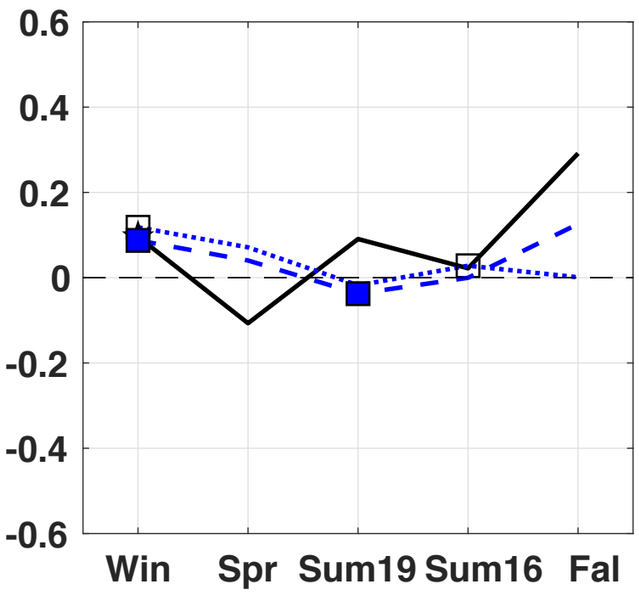

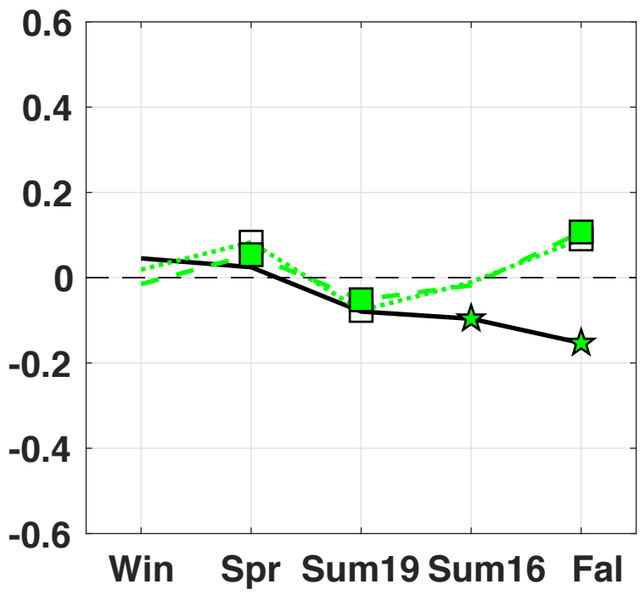

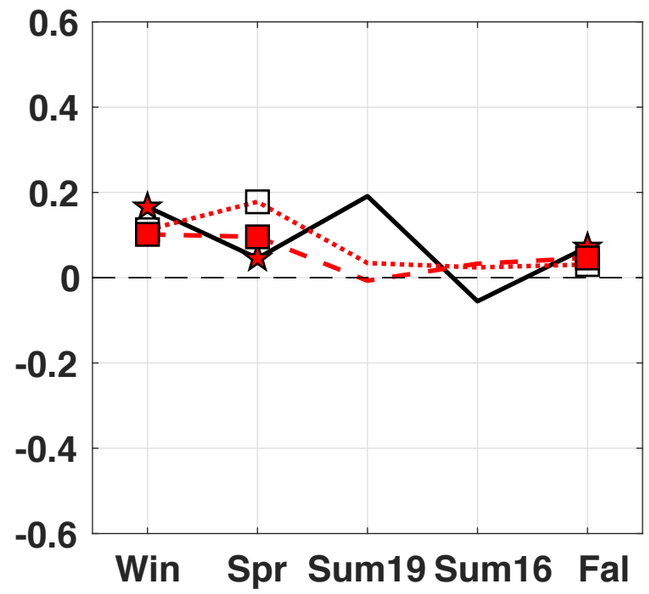

Regression Slope Between ΔCO_2 and ΔCOS

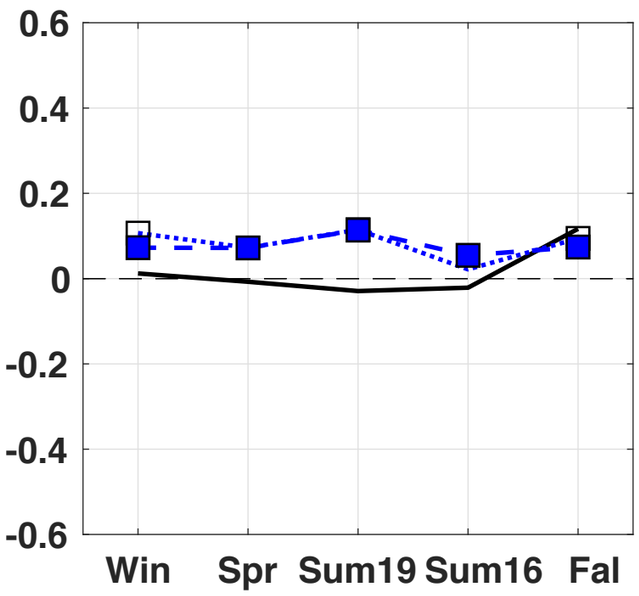

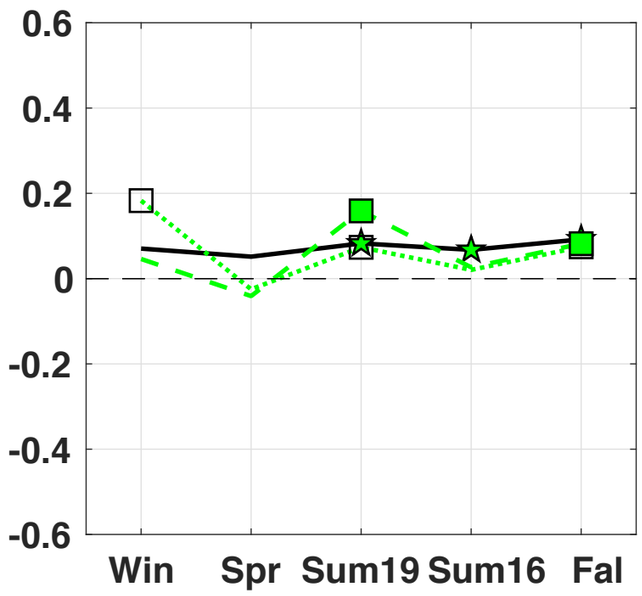

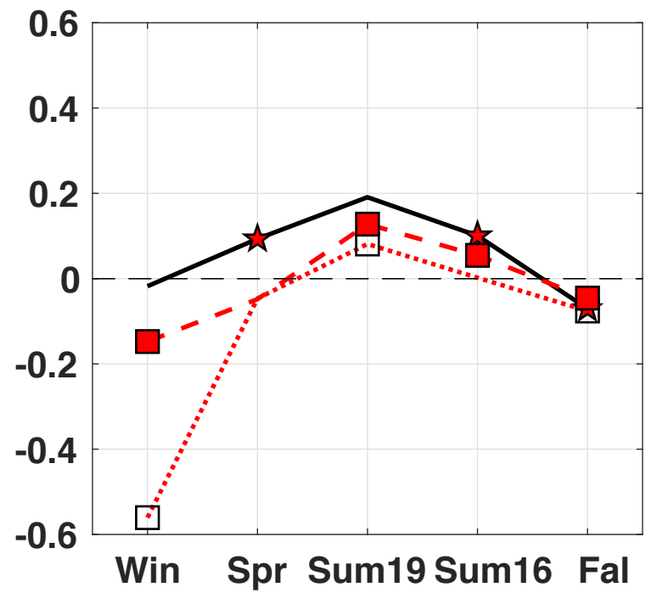

Regression Slope Between ΔCOS and ΔCO

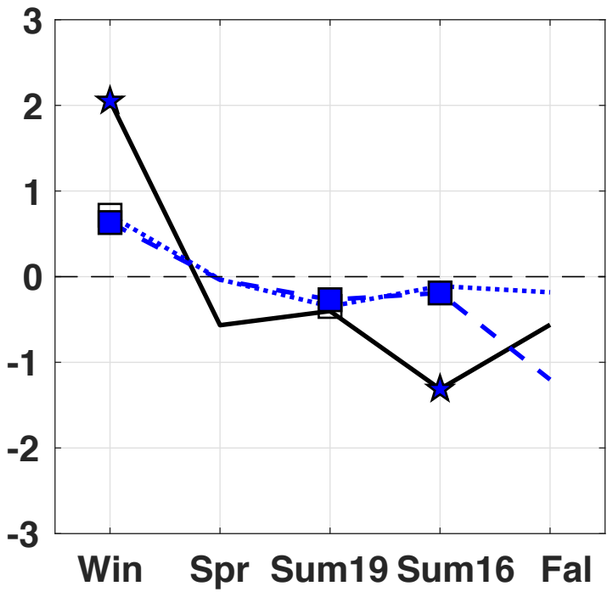

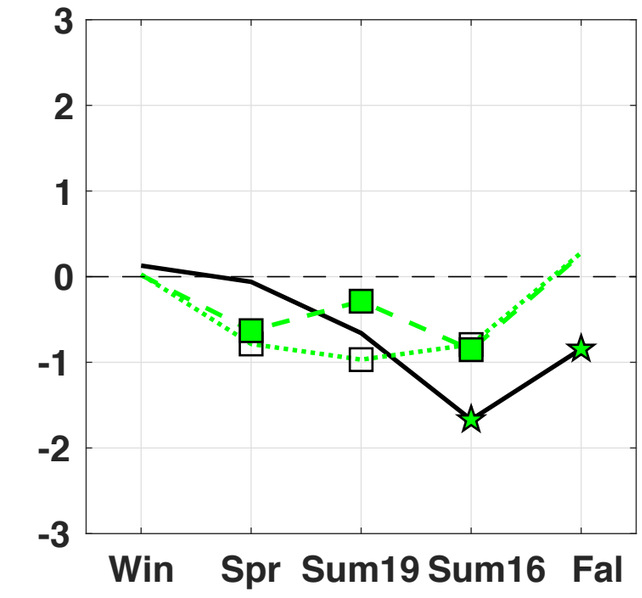

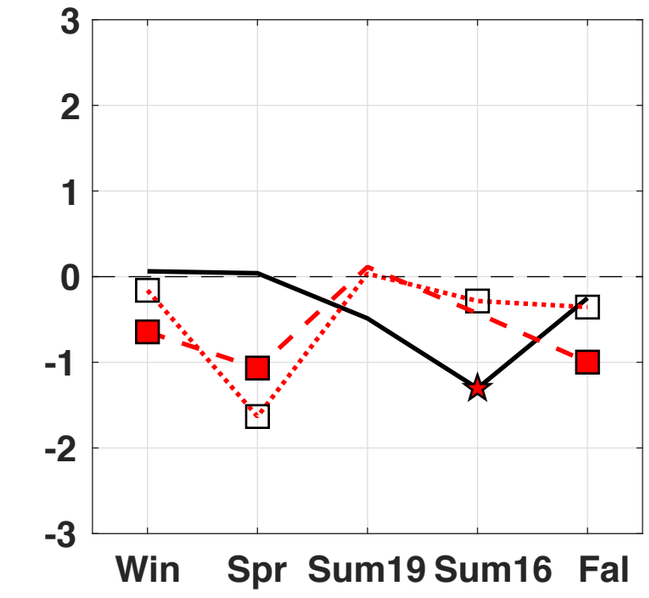

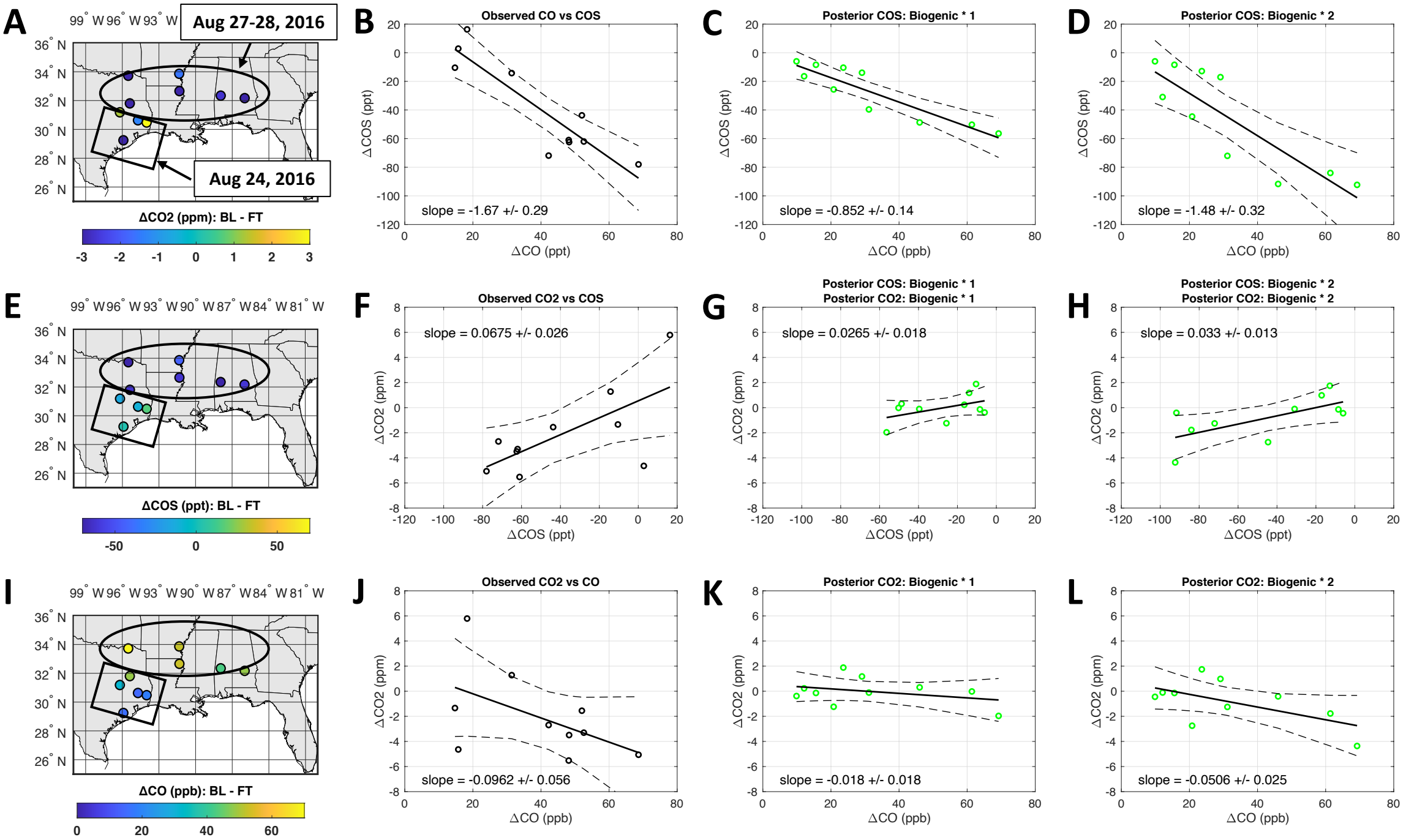
A
99° W 96° W 93° W
36° N
34° N
32° N
30° N
28° N
26° N
Aug 27-28, 2016
Aug 24, 2016
ΔCO2 (ppm): BL - FT
-3 -2 -1 0 1 2 3
B
Observed CO vs COS
ΔCOS (ppt)
ΔCO (ppt)
slope = -1.67 +/- 0.29
C
Posterior COS: Biogenic * 1
ΔCOS (ppt)
ΔCO (ppb)
slope = -0.852 +/- 0.14
D
Posterior COS: Biogenic * 2
ΔCOS (ppt)
ΔCO (ppb)
slope = -1.48 +/- 0.32
E
99° W 96° W 93° W 90° W 87° W 84° W 81° W
36° N
34° N
32° N
30° N
28° N
26° N
ΔCOS (ppt): BL - FT
-50 0 50
F
Observed CO2 vs COS
ΔCO2 (ppm)
ΔCOS (ppt)
slope = 0.0675 +/- 0.026
G
Posterior COS: Biogenic * 1
Posterior CO2: Biogenic * 1
ΔCO2 (ppm)
ΔCOS (ppt)
slope = 0.0265 +/- 0.018
H
Posterior COS: Biogenic * 2
Posterior CO2: Biogenic * 2
ΔCO2 (ppm)
ΔCOS (ppt)
slope = 0.033 +/- 0.013
I
99° W 96° W 93° W 90° W 87° W 84° W 81° W
36° N
34° N
32° N
30° N
28° N
26° N
ΔCO (ppb): BL - FT
0 20 40 60
J
Observed CO2 vs CO
ΔCO2 (ppm)
ΔCO (ppb)
slope = -0.0962 +/- 0.056
K
Posterior CO2: Biogenic * 1
ΔCO2 (ppm)
ΔCO (ppb)
slope = -0.018 +/- 0.018
L
Posterior CO2: Biogenic * 2
ΔCO2 (ppm)
ΔCO (ppb)
slope = -0.0506 +/- 0.025